

MODELING THE COMBINED EFFECTS OF DETERMINISTIC AND STATISTICAL STRUCTURE FOR OPTIMIZATION OF REGIONAL MONITORING

Vernon F. Cormier, et al.

**Physics Department
University of Connecticut
2152 Hillside Road, U-3046
Storrs, CT 06269-3046**

30 June 2015

Final Report

APPROVED FOR PUBLIC RELEASE; DISTRIBUTION IS UNLIMITED.



**AIR FORCE RESEARCH LABORATORY
Space Vehicles Directorate
3550 Aberdeen Ave SE
AIR FORCE MATERIEL COMMAND
KIRTLAND AIR FORCE BASE, NM 87117-5776**

DTIC COPY

NOTICE AND SIGNATURE PAGE

Using Government drawings, specifications, or other data included in this document for any purpose other than Government procurement does not in any way obligate the U.S. Government. The fact that the Government formulated or supplied the drawings, specifications, or other data does not license the holder or any other person or corporation; or convey any rights or permission to manufacture, use, or sell any patented invention that may relate to them.

This report was cleared for public release by the 377 ABW Public Affairs Office and is available to the general public, including foreign nationals. Copies may be obtained from the Defense Technical Information Center (DTIC) (<http://www.dtic.mil>).

AFRL-RV-PS-TR-2015-0144 HAS BEEN REVIEWED AND IS APPROVED FOR PUBLICATION IN ACCORDANCE WITH ASSIGNED DISTRIBUTION STATEMENT.

//SIGNED//

Dr. Robert Raistrick
Project Manager, AFRL/RVBYE

//SIGNED//

Glenn M. Vaughan, Colonel, USAF
Chief, Battlespace Environment Division

This report is published in the interest of scientific and technical information exchange, and its publication does not constitute the Government's approval or disapproval of its ideas or findings.

REPORT DOCUMENTATION PAGE				Form Approved OMB No. 0704-0188	
Public reporting burden for this collection of information is estimated to average 1 hour per response, including the time for reviewing instructions, searching existing data sources, gathering and maintaining the data needed, and completing and reviewing this collection of information. Send comments regarding this burden estimate or any other aspect of this collection of information, including suggestions for reducing this burden to Department of Defense, Washington Headquarters Services, Directorate for Information Operations and Reports (0704-0188), 1215 Jefferson Davis Highway, Suite 1204, Arlington, VA 22202-4302. Respondents should be aware that notwithstanding any other provision of law, no person shall be subject to any penalty for failing to comply with a collection of information if it does not display a currently valid OMB control number. PLEASE DO NOT RETURN YOUR FORM TO THE ABOVE ADDRESS.					
1. REPORT DATE (DD-MM-YYYY) 30-06-2015		2. REPORT TYPE Final Report		3. DATES COVERED (From - To) 04 Jun 2012 – 30 June 2015	
4. TITLE AND SUBTITLE Modeling the Combined Effects of Deterministic and Statistical Structure for Optimization of Regional Monitoring				5a. CONTRACT NUMBER FA9453-12-C-0207	
				5b. GRANT NUMBER	
				5c. PROGRAM ELEMENT NUMBER 62601F	
6. AUTHOR(S) Vernon F. Cormier, Christopher J. Sanborn, Michele Fitzpatrick, Steven Walsh, and Nil Mistry				5d. PROJECT NUMBER 1010	
				5e. TASK NUMBER PPM00014476	
				5f. WORK UNIT NUMBER EF007739	
7. PERFORMING ORGANIZATION NAME(S) AND ADDRESS(ES) Physics Department University of Connecticut 2152 Hillside Road, U-3046 Storrs, CT 06269-3046				8. PERFORMING ORGANIZATION REPORT NUMBER	
9. SPONSORING / MONITORING AGENCY NAME(S) AND ADDRESS(ES) Air Force Research Laboratory Space Vehicles Directorate 3550 Aberdeen Avenue SE Kirtland AFB, NM 87117-5776				10. SPONSOR/MONITOR'S ACRONYM(S) AFRL/RVBYE	
				11. SPONSOR/MONITOR'S REPORT NUMBER(S) AFRL-RV-PS-TR-2015-0144	
12. DISTRIBUTION / AVAILABILITY STATEMENT Approved for public release; distribution is unlimited. (377ABW-2015-0658 dtd 17 Aug 2015)					
13. SUPPLEMENTARY NOTES					
14. ABSTRACT The differences between earthquakes and explosions are largest in the highest recordable frequency band. In this band, scattering of elastic energy by small-scale heterogeneity (less than a wavelength) can equilibrate energy on components of motion and stabilize the behavior of the Lg wave trapped in the Earth's crust. Larger-scale deterministic structure (greater than a wavelength) can still assume major control over the efficiency or blockage of the Lg and other regional/local seismic waves. This project models the combined effects of the large-scale (deterministic) and the small scale (statistical) structure to invert for improved structural models and to evaluate the performance of yield estimators and discriminants in the region of the Lop Nor test site. This is accomplished by synthesizing seismograms using a radiative transport technique to predict the high frequency coda (2 to 4 Hz) of regional seismic phases at stations having known large-scale three-dimensional structure, combined with experiments to estimate the effects of multiple-scattering from unknown small-scale structure. We describe a code to shoot body wave rays through general deterministic 3-D structure, including the coda envelope sensitivities to parameters describing the heterogeneity spectrum, intrinsic attenuation, Moho transition, and tectonic release of nuclear tests. We predict that discriminants in this region based on P/Lg amplitude ratios will best separate earthquake and explosion populations at frequencies 2 Hz and higher.					
15. SUBJECT TERMS seismic scattering, radiative transport, stochastic scattering, regional seismic phase amplitudes					
16. SECURITY CLASSIFICATION OF:			17. LIMITATION OF ABSTRACT Unlimited	18. NUMBER OF PAGES 48	19a. NAME OF RESPONSIBLE PERSON Dr. Robert Raistrick
a. REPORT Unclassified	b. ABSTRACT Unclassified	c. THIS PAGE Unclassified			19b. TELEPHONE NUMBER (include area code)

This page is intentionally left blank.

Table of Contents

1. Summary	1
2. Introduction.....	1
2.1 The importance of very high frequency coda modeling	1
2.2 Limitations of numerical modeling: high frequency and long range.....	2
2.3 Importance of large-scale structure and limitations of path calibrations.....	2
3. Technical Approach	3
3.1 Radiative transport	3
3.2 Advantages of radiative transport	5
3.3 Construction of models	6
3.4 Software package	7
4. Results and Discussion	14
4.1 Lop Nor region: Deterministic Model and Data	14
4.2 Sensitivity of Coda Envelopes to Statistical Parameters.....	17
4.3 Intrinsic Q effects.....	26
4.4 Surface layer effects.....	27
4.5 Pn and Sn	28
4.6 Synthetics compared with data by frequency band.....	31
4.7 Tectonic release: regional propagation effects	32
5. Conclusions.....	34
References.....	35
List of Symbols, Abbreviations, and Acronyms	38

Figures

Figure 1. Radiative transport algorithm and heterogeneity spectra	4
Figure 2. Examples of deterministic and statistical structure	7
Figure 3. Time snapshots of regional seismic wavefield versus range and depth	10
Figure 4. Example coda envelopes for earthquakes and explosions synthesized by radiative transport.	11
Figure 5. Example coda envelopes displayed as travel time versus distance plots	12
Figure 6. Lop Nor test site region and paths to seismic stations MAK and WUS.....	15
Figure 7. Vertical component bandpassed data recorded at WUS and MAK from the Lop Nor region.....	16
Figure 8. Simplified Lop Nor region earth model	17
Figure 9. Coda envelope synthetics for earthquakes in the Lop Nor region for a reference heterogeneity spectrum.	19
Figure 10. Mean free path and dipole projection for velocity perturbations	20
Figure 11a. Earthquake (left) and explosion (right) coda envelopes for low epsilon.....	20
Figure 11b. Earthquake (left) and explosion (right) coda envelopes for high epsilon.	21
Figure 12. Mean free path and dipole projection for density perturbations.....	22
Figure 13. Synthetic coda envelopes for density perturbations	22
Figure 14. Mean free path and dipole projection for variable scale lengths of a von Karman spectrum.	23
Figure 15. Synthetic coda envelopes for variable scale lengths of a von Karman spectrum.....	24

Figure 16. Mean free path and dipole projection for the Hurst parameter k , which controls spectral shape for wavelengths larger than the scale length of a von Karman spectrum...	25
Figure 17. Synthetic coda envelopes for earthquakes and explosions with and without intrinsic attenuation.....	26
Figure 18. Synthetic coda envelopes for earthquakes and explosions with and without a thin sediment layer.	28
Figure 19. Cross-section of an Earth model having a Moho transition specified by a series of stair-step layers.....	29
Figure 20. Lop Nor paths to MAK and WUS and source mechanism of a southern Xinjiang earthquake.	29
Figure 21. Synthetic coda envelopes for earthquakes and explosions in a Lop Nor model having a Moho transition.	30
Figure 22. Comparison of 2 Hz synthetics with observed waveforms and passed for 2 Hz.	30
Figure 23. Synthetic coda envelopes compared with data recorded at MAK for a series of frequencies.....	31
Figure 24. Synthetic coda envelopes for nuclear tests with tectonic release compared with observed data for Lop Nor nuclear tests at a series of narrow frequency bands.	33

1. SUMMARY

Discriminants based on the differences in the seismic source spectrum between earthquakes and explosions often work best in the highest recordable frequency band (e.g., Walter et al., 1995; Allmann et al., 2008). In this high frequency band, ($> 2\text{--}4$ Hz) scattering of elastic energy by small-scale heterogeneity (less than a wavelength) can equilibrate energy on all components of motion and stabilize the behavior of yield measures based on the Lg wave trapped in the Earth's crust. Lateral variation of both small-scale heterogeneity and larger-scale, resolvable structure (greater than a wavelength) can control the blockage of Lg and the amplitude of other regional seismic waves (Cao and Muirhead, 1993; Sens-Schonfelder et al., 2009). This project models the combined effects of the large-scale (deterministic) and the small scale (statistical) structure to invert for improved structural models and to evaluate the performance of yield estimators and discriminants at selected seismic stations in Eurasia. These tasks are approached by synthesizing seismograms using a radiative transport technique to predict the high frequency coda (>5 Hz) of regional seismic phases at stations having known large-scale three-dimensional structure, combined with experiments to estimate the effects of multiple-scattering from unknown small-scale structure. We describe a radiative transport code and report the results of its use in modeling regional wave propagation, including tests of sensitivity of the shapes of high frequency seismic coda shapes to structural and source parameters in the Lop Nor, China region.

2. INTRODUCTION

This section motivates the needs of CTBT monitoring for modeling high-frequency seismic waveforms in 3-D structures at ranges much longer than 100 wavelengths. Section 3 describes how a radiative transport algorithm can fulfill this need and outlines our development and implementation of such an algorithm with an open-source computer code. Section 4 presents results of experiments that vary deterministic and statistical parameters of Earth models as well as source radiation patterns, depth, and tectonic release. Concluding remarks are presented in Section 5.

2.1 The importance of very high frequency coda modeling

Differences in source properties between a theoretically ideal earthquake and explosion are well understood: distributed slip on a fault plane versus an approximate step-function in pressure applied to a spherical cavity deep enough for explosion containment (Brune, 1970; Mueller and Murphy, 1971). These simple theories do not incorporate dynamically triggered fault motion, complex surfaces of equivalent explosion volumes, and explosive tectonic release. Nevertheless they are good enough to accurately predict that an earthquake with the same scalar moment will have much higher corner frequency in its displacement spectrum. The success of common seismic discriminants based on amplitude ratios in different group velocity windows (e.g., Pg/Lg) depend as much on this spectral difference as they do on differences in source depth and P and S radiation patterns (Walter et al., 2009).

High frequency Lg coda has also been shown to be useful for yield estimation (e.g., Mayeda, 1993). As frequency increases, however, it becomes increasingly difficult to obtain perfect knowledge of small-scale structure needed to predict a seismogram of an earthquake or an explosion wiggle for wiggle. Yet even without this knowledge, simple statistical descriptions of medium properties can be used to predict the shape of high frequency Lg coda.

2.2 Limitations of numerical modeling: high frequency and long range

Given the importance of high frequencies to seismic monitoring, it would be desirable to model high frequency regional seismograms with enough computational efficiency that many structural and source models could be routinely tested and compared against observations within several hours or less. Unfortunately, even with the advance of parallel computation and increased access to large clusters of processors, numerical modeling in three-dimensional earth models rarely exceeds ranges of several hundred wavelengths for computing times less than 1 day. At 5 Hz this range is typically less than 100-200 km, which is valuable to predictions of earthquake strong ground motion, but more limited in value to nuclear monitoring where IMS stations may be 1000 km or further from regions of interest in Eurasia.

2.3 Importance of large-scale structure and limitations of path calibrations

Given the apparent success of discriminants and yield estimators from high frequency coda with minimal knowledge of earth structure and source descriptions, one may believe that monitoring is purely a problem of calibrating coda measurements and amplitude ratios along paths to each monitoring station, applying spatial interpolators (e.g., kriging, Fan et al., 2002) and a model of propagation in a plane-layered medium (e.g., MDAC, Taylor et al., 2002). Many examples, however, have been collected in which sharp gradients in the Moho depth, mountain roots, and deep sedimentary basins have strongly affected azimuthal variations in the character and detection of regional seismic phases (e.g., Ruzaiкин et al., 1971), making simple propagation models and path interpolation unreliable tools for predicting waveform behavior.

The effects of larger-scale (greater than a wavelength) structure will hence limit the portability of discriminants and yield estimators and limit the effectiveness of their path interpolations and calibrations. In addition to these operational concerns, a number of fundamental problems involving the interaction of large with smaller-scale (wavelength and smaller) structure have also not been well investigated:

- Can large-scale structures always block the highest detectable frequency of some regional phases?
- Is there a frequency band on Earth in which the effects on regional seismograms of large-scale structure disappear?
- How important is small-scale structure in the vicinity of large-scale structure?

- Is anisotropy of the scale-lengths of small-scale structure (horizontally or vertically stretched heterogeneity) important to regional phase propagation?

By combining the effects of large-scale and small-scale structure in a computationally efficient 3-D method of seismogram synthesis based on the radiative transport approach, our project seeks to determine small-and large-scale 3-D structure in the vicinity of selected monitoring stations by matching the coda of very high frequency (> 5 Hz) regional phases. The results of this modeling will be used to optimize coda-based yield estimators and discriminants as a function of azimuth to these stations.

3. TECHNICAL APPROACH

3.1 Radiative Transport

Radiative transport seeks to model the diffusive transport of energy through processes of multiple scattering in a medium having random fluctuations in physical properties. Its earliest and most extensive applications are to the propagation of electromagnetic waves, especially to the description of stellar images and scintillation (Chandrasekhar, 1960). Wu (1985) introduced radiative transport to seismology, modeling the coda, or envelope of energy, starting and following elastic P and S waves. By including multiple-scattering, radiative transport improved upon the single scattering, Rayleigh-Born, model of seismic coda introduced by Aki and Chouet (1975). An early significant result of Wu's work with radiative transport is that multiple scattering often becomes the dominant mechanism controlling coda shapes at frequencies above 5 Hz on Earth, explaining a spindle-shaped (lunar-like) coda observed in this frequency band. Reviews of seismic radiative transport modeling include the text by Sato and Fehler (1998) and a monograph by Margerin (2004). Przybilla, et al. (2009) has compared the method against finite-difference synthetics in 2-D, validating body wave coda predictions of the radiative transport method.

Following Shearer and Earle (2008), an algorithm to implement radiative transport can be described in a few simple steps:

- (1) Choose a heterogeneity power spectrum for the medium (the heterogeneity power spectrum is the Fourier transform of the spatial autocorrelation of small-scale heterogeneity).
- (2) From the heterogeneity spectrum, calculate the scattering coefficient, g , which is the scattering power per unit volume.
- (3) Average g for P and S waves over all angles, forming, for example, $g_o = 1/l_p$, where path l_p is the mean free path of a P wave.

- (4) Calculate path length r , assuming r is an exponentially distributed random number having a mean value l_p for P waves and l_s for S waves respectively, i.e, $r_p = -\ln(x)$, where x is a random number between 0 and 1.
- (5) Choose the scattered direction from sampling a probability density taken from the Born scattering coefficients of the heterogeneity model (Sato and Fehler, 1998) and continue computing the path of the scattered energy packet. Random numbers sampling a scatter radiation pattern are used to determine whether the scattering is into P or S and to determine S polarization.

Figure 1 shows how multiply scattered packets of elastic energy are tracked starting and their relation to a statistical realization of small-scale heterogeneity.

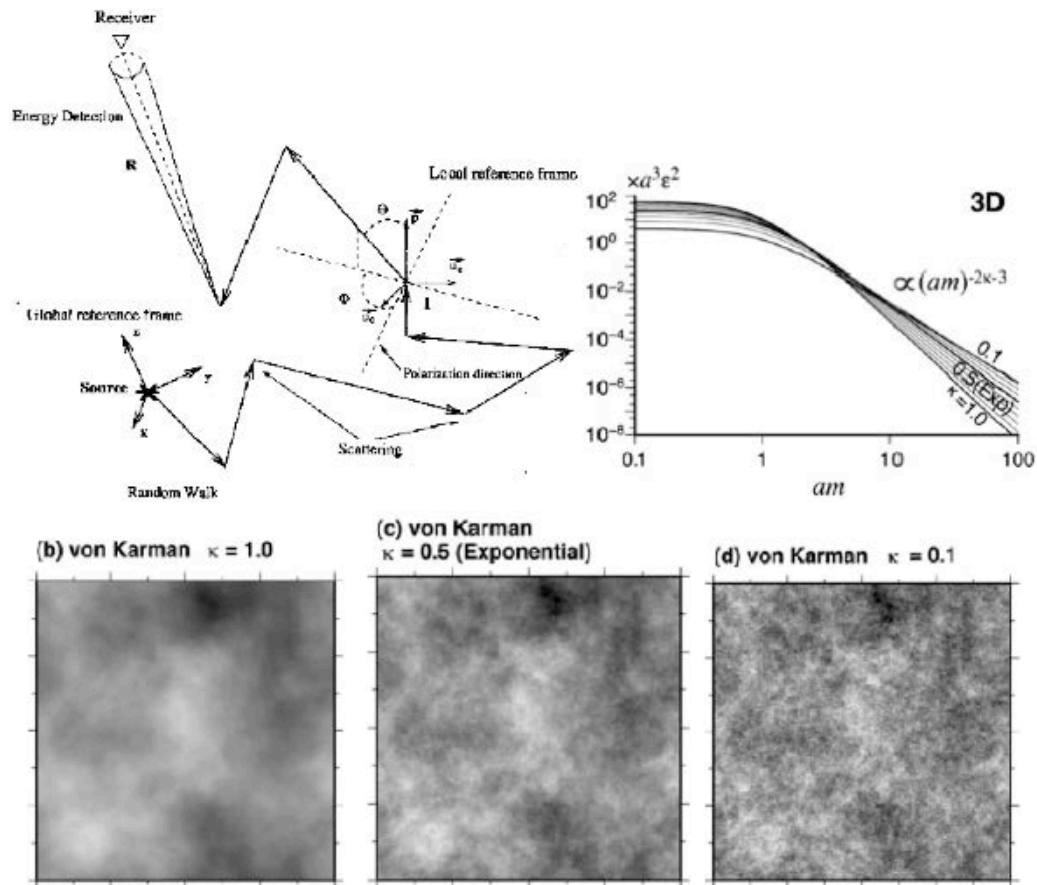


Figure 1. Radiative transport algorithm and heterogeneity spectra. *Top left: random walk along ray paths of packets of elastic energy scattered by heterogeneity having a wavenumber spectrum (top right) parameterized by a scale length a after which small spatial scales by varying powers of ka (ma) where $k = 2\pi/\text{wavelength}$. Bottom: example spatial realizations of heterogeneity spectra.*

3.2 Advantages of Radiative Transport

The principle advantage of radiative transport is the ability to simulate the effects of small-scale structure without the need for model meshes that are dense enough to explicitly describe that structure. Instead, the model mesh describes only the large-scale, long-wavelength equivalent, background medium, against which small-scale heterogeneities are assumed as a random perturbation field. The small-scale heterogeneities are described in the aggregate via a small number of statistical parameters, rather than describing the perturbation field explicitly in fine detail. This represents a dramatic reduction in the storage requirements needed to describe the Earth model. Additionally, since radiative transport is not a numerical wave-equation solver, it also avoids the requirement for a simulation using a grid dense enough to capture the temporal and spatial derivatives in the full equations of motion. Thus, models are described with what we call a “model mesh” rather than a “simulation grid,” where the model features determine the necessary mesh density we wish to capture, rather than the wavelengths we wish to simulate. In contrast, high-order numerical finite difference methods might require as many as 10 to 50 grid points per wavelength. This would quickly become a limiting factor on the spatial extent of models, making unfeasible routine modeling of seismic waves that exceed several 100 wavelengths of 3-D propagation

This sparse-mesh advantage depends on the ability to categorically separate structure into large and small scales. In general, the distinction is made by comparison of the feature size to the wavelength being simulated. Large structure is that for which $ka \gg 1$, where a is a typical feature size and k is the wavenumber corresponding to the chosen wavelength, and small scale is, for radiative transport purposes, structure for which $ka \sim 1$, which is the regime in which scattering is most pronounced. Radiative transport simulations are usually carried out at a single frequency, and this choice of frequency establishes the reference size for this distinction. Our frequency range of interest is the 1 Hz to 10 Hz band, which at typical seismic velocities of 3 to 8 km/s, establishes “small scale” in the approximate range of 0.3 km to 8.0 km or smaller, and means that node spacing on our model meshes can be much larger than that.

For practical modeling purposes, large-scale structure is that which comes from published velocity models of the Earth, in which seismic wave velocities have been imaged from receiver functions, travel-times, and waveforms inversions. Typically, these images are determined from longer wavelength signals than the high-frequency signals that are of interest regional nuclear monitoring. These inversions image the long-wavelength equivalent or composite medium average seismic velocities. These large-scale velocity maps then form the background structure against which small-scale heterogeneities are assumed as a perturbation field, for use in generating higher-frequency synthetics. The advantage of radiative transport is the ability to describe this perturbation field statistically and to simulate it stochastically, rather than deterministically, even as the large-scale structure is handled by deterministic ray tracing in the background, long-wavelength equivalent, model.

The practical mesh fineness required to describe deterministic structure is application-specific, and can vary quite a bit. Node spacings of 10's to 100's of kilometers for lateral variations, and five to 20 kilometers for vertical variation, could be considered well within the range of typical. Scales as small as 1 km, however, might be needed to describe lateral variations in important sharp, well-resolved, crustal discontinuities, such as the Moho. A typical scale length for the material heterogeneities that become the stochastic perturbation field might easily span 0.01 to 10.0 kilometers. If features of these, unresolved, smaller scale lengths were to be described explicitly, the model mesh storage requirements would increase by many orders of magnitude.

3.3 Construction of Models

Earth models consist of a background deterministic component, consisting of first-order discontinuities with topography separating layers having a 3-D variation of and velocities and densities interpolated over a coarse grid, and a perturbed statistical component, specified by a heterogeneity spectrum having parameters specifying the power of velocity and density fluctuation and the shape of this spectrum as a function of wavenumber (Figures 1 and 2).

Frankel and Clayton (1986) demonstrated how earth models can be constructed that have a specified heterogeneity spectrum. The procedure consists in having perturbations at knot points driven by a random number generator, Fourier transforming the spatial model into the wavenumber domain, filtering by a desired wavenumber spectral shape, and inverse Fourier transforming back to space.

Since Frankel and Clayton's original work, advances have occurred in statistical characterization and understanding of small-scale geologic heterogeneity. Goff et al. (1994) described a procedure by which models having the spatial statistics of polycrystalline or multi-modal assemblages of rocks can be generated. Work beginning with Levander et al. (1994) and Pullammanappallil et al. (1997) makes it possible to formulate statistical models for common sedimentary and metamorphic formations. Model statistics can be modified as needed to reproduce the three-component behavior of the coda of regional seismic phases. Strong emphasis is placed on correctly characterizing the statistics of small-scale heterogeneities in the upper, highly heterogeneous, 5 km of the earth. Small-scale statistics affect the partitioning of P and S energy on the three-components of motion by the effects of scattering near the source and receiver and hence the performance of discriminants tuned to differences in sources occurring at the depths of contained nuclear tests.

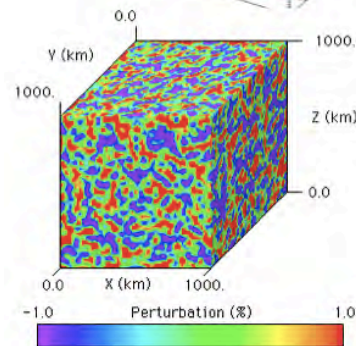
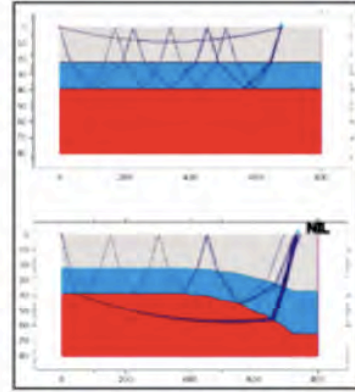
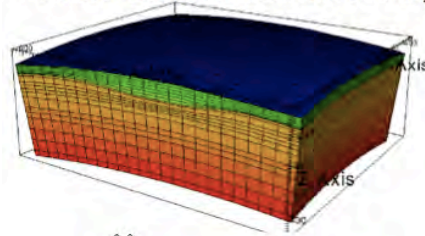
Lateral variations in crustal thickness, basin depths, mountain roots, and lateral tectonic transitions significantly affect the phases used for discrimination and detection. One example is the study by Pedersen et al. (1998), who explain anomalous Rayleigh to Love mode conversion from Lop Nor explosions by changes in crustal thickness at the boundary of the Tarim Basin and Tian Shan mountain belt. Moho topography and basin thickness can also strongly affect the propagation of Lg (Cormier and Anderson, 2004). The scale of these types of lateral structural variations is often large enough to be resolvable by local and regional reflection and refraction experiments, gravity and

magnetic data, regionalization by surficial geology, and global surface wave inversions, e.g., Figure 2. Hence, we refer to these types of structures as deterministic. The types of data used to infer deterministic structure are collected at widely different spatial scales, presenting a challenge to the parameterization of a three-dimensional model appropriate for a region surrounding a particular seismic station. The parameterization should be flexible enough to be specified at high resolution where data is available and at lower resolution where it is not. Resolution should be high to describe features important to regional wave propagation, such as Moho and basin topography, but can be lower near interfaces having smaller velocity contrasts and lower with increasing depth in the mantle, where heterogeneity power decreases.

DETERMINISTIC STRUCTURE

Examples:

- Changes in Moho depth
- Lateral variation in seismic velocity



STATISTICAL STRUCTURE

Example:

- fine-scale deviations of seismic velocity, due to material inhomogeneity, small cracks and fissures, etc. Random heterogeneity can be parameterized by scale-length and strength parameters.

Figure 2. Examples of deterministic and statistical structure. *Top: examples of known (deterministic) large-scale heterogeneity and its effects on S and Lg waves (multiple critically reflected S waves at the Moho). Bottom: example of a realization of 3-D small-scale (statistically described) heterogeneity.*

3.4 Software Package

3.4.1 Implementation and relation to existing codes

We have developed a new software package for synthetic seismogram generation called *Radiative3D* — *A code for radiative transport in 3D Earth models*. (Homepage: <https://rainbow.phys.uconn.edu/geowiki/Radiative3D>) *Radiative3D* is a comprehensive new code with flexible Earth model entry, moment-tensor based source modeling, and receiver and array modeling. The simulation engine includes deterministic ray tracing for longitudinal and shear propagation modes in linear velocity gradients, stochastic scattering controlled by heterogeneity parameters, reflection and transmission handling at

sharp boundaries, and attenuation modeling from internal friction. Visualization and post-processing tools have been created to produce seismic envelopes, travel-time curves, and three-dimensional body-wave visualizations of energy propagation from Radiative3D output. Radiative3D will be made available to the scientific community as a free and open-source software product. Radiative3D is a new code that takes major inspiration from two prior codes, namely Raytrace3d (Menke, 2002) and PSPhonon (Shearer and Earle, 2004). Raytrace3D solves ray propagation in a 3-D velocity model, and PSPhonon performs radiative transport, including scattering, in a 1-D layered-earth model. Our code performs both tasks in a full 3-D model.

In our implementation, elastic energy is considered to originate from a source event at a fixed location and time. A quantum of that energy is then propagated as a discrete packet or bundle, which we refer to as a phonon (in analogy to the particle representation of light as a stream of photons). A phonon's path through an Earth model is determined by a combination of ray theory to handle the deterministic propagation through the composite medium background structure (large scale structure, capturing broad variations in elastic properties), and by scattering theory, which is the stochastic handling of scattering due to small-scale heterogeneities, assumed as perturbations to the background structure. A scattering event is, in essence, an interruption and randomization of a particle's otherwise deterministic progress. With a sufficient number of phonons emitted from the source event, a picture of the energy transport throughout the model begins to emerge. Records of the phonon travel paths can be used either in bulk or via selection criteria to visualize this energy transport. In bulk, the data can be used to produce movies or still-frames of the evolving wavefront throughout the three-dimensional model. Via selection criteria, just those phonons that, for example, interact with the surface within a specified gather radius of a hypothetical seismometer can be collected and used to produce seismic waveforms of surface movement at the given location. With a sufficient quantity of virtual seismometers, travel-time curves can also be produced.

3.4.2 Capabilities of Radiative3D

Source modeling: Radiative3D uses a moment-tensor representation to describe seismic sources. Moment tensor representation is a truncation at quadrupole order of the multipole expansion of the elastic wave field at large distances from the source, and thus provides a way to parameterize complex sources as point-source equivalents. Despite discarding higher-order multipoles, moment tensors provide good representation of a wide range of naturally occurring and man-made seismic sources. Both idealized shear dislocation (e.g. slip on a fault plane) and idealized explosions are exactly representable by moment tensors. In fact, the six degrees of freedom in the rank-2 symmetric moment tensor allow for the specification of a full range of event types from pure isotropic (explosion/implosion), to double couple (shear-dislocation earthquake), and various other configurations such as compensated linear vector dipole (CLVD), etc. Internally, the moment tensor is converted into probability distributions describing the likelihood of phonon emission at various take-off angles from the event source.

Scattering shapes: A scattering event involves an interruption of the phonon ray path at a scattering location and a re-radiation of the phonon at a deflected angle. The angular dependence of scattering is determined by the scattering radiation patterns described in Sato and Fehler (1998, chapter 4). These radiation patterns depend on frequency and on four statistical parameters describing the heterogeneity, as well as on the background P and S elastic velocities. The four statistical parameters include the strength ε of the perturbation field, the scale length a that defines a low-pass corner in the power spectrum of length scales, a parameter κ that determines the fall-off rate of the power spectrum, and a parameter ν that establishes a ratio between velocity and density fluctuation strengths. Like event sources, the scattering shapes are also represented internally as probability distributions characterizing the relative likelihood of various deflection angles.

Flexible Earth model input: Radiative3D supports Earth models based on a multitude of model construction metaphors, allowing both very simple and very complex models to be constructed with ease. One supported model type is the layered-Earth model, in which the model consists of consecutive layers at increasing depth. Unlike traditional layered Earth models, however, a degree of lateral variation is supportable by the ability of the interfaces between layers to take on arbitrary orientation. Thus, for example, gradually broadening or gradually tapering crust structures can be modeled. In layered models, the material properties (elastic velocities, density, heterogeneity spectra, and intrinsic attenuation) are uniform throughout the layer. Gradients in properties, e.g. velocity gradients, must be simulated in stair-step fashion. An Earth-coordinate subsystem (ECS) allows model parameters, event locations, and seismometer locations to be specified in a coordinate system of the user's choice and automatic conversion to layered internal model space will occur. The ECS also allows Earth-flattening transformations to be applied as a user option, to simulate Earth curvature in layered models.

For more sophisticated topographical or laterally varying models, Radiative3D also supports models composed of tetrahedra, allowing full three-dimensional models to be specified. In tetrahedral models, properties are specified on the corners of the tetrahedra, and are linearly interpolated throughout the volume of the tetrahedron. Thus velocity gradients can be simulated directly. Additionally, values are continuous across tetrahedral boundaries, unless the boundary represents a sharp discontinuity, which is also supported by the software. At present, the tetrahedral functionality of Radiative3D has been recently completed but is still in testing phase. Tools to help the construction of complex models for input to the software are also under development.

Signal output: Radiative3D has two basic output modes. The first is a play-by-play event stream that reports everything that happens to a phonon from generation at the source event until eventual phonon-death as the phonon either leaves the model boundaries, or is abandoned after its lifetime exceeds the window of interest. This mode can be used for volumetric visualization of energy propagation throughout the whole model. The second output stream is the time-binned signals from virtual seismometers that collect and report on the energy accumulated at fixed points on the model surface.

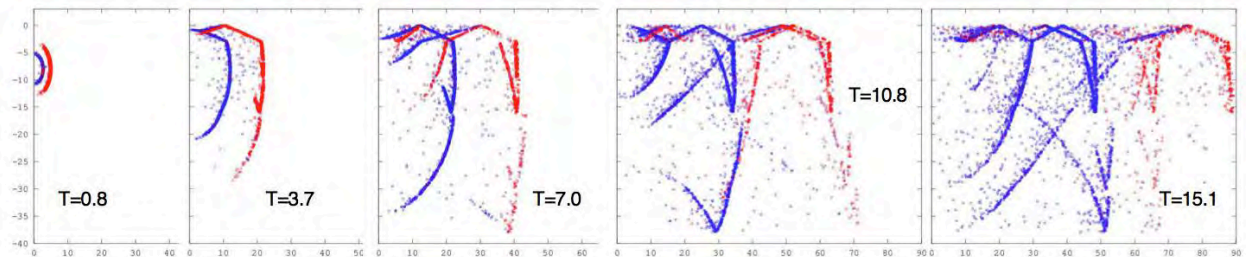
These can be used to generate synthetic seismograms (as energy envelopes) or synthetic travel-time curves.

3.4.3 Visualizing Output

Radiative3D produces output suitable for visualization with external tools. The output capabilities fall into two major categories: (1) event reporting, and (2) seismic energy binning. Event reporting means reporting the progress of individual phonons in a play-by-play manner. Examples of “events” in this context include: generation, scattering, crossing a model boundary, free-surface or discontinuity interface reflection and transmission, etc. When these events are analyzed in post-processing, detailed pictures of energy propagation can be constructed. One of the first visualization tools developed was a GNU Octave script to produce videos illustrating P and S energy propagation in the Earth model.

Figure 3 shows energy propagation visualized as a time series plot of phonon locations in a model cross section. Red dots represent P phonons, blue dots represent S phonons. Reflection and refraction occurs at interfaces between model layers at which velocities are discontinuous. Conversions between P and S polarization are driven by both scattering and reflection/transmission events.

Earthquake Time-Series:



Explosion Time-Series:

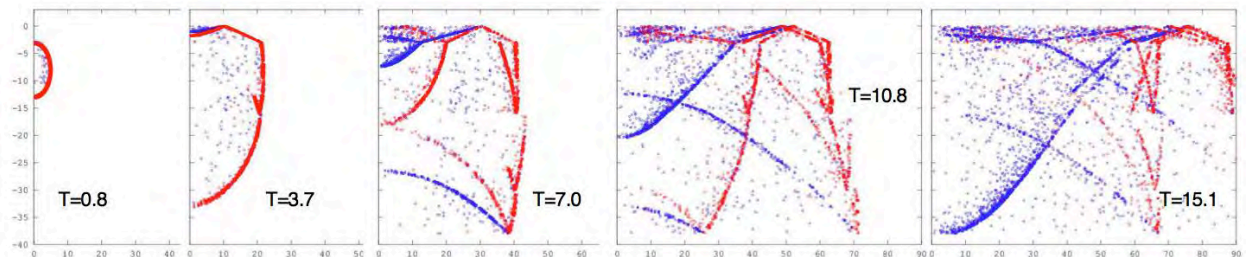


Figure 3. Time snapshots of regional seismic wavefield versus range and depth. *Energy propagation visualized as a time series plot of phonon locations in a model cross section. Note the initial absence of the S wavefronts (blue) in the explosion time-series and its progressive development with time due to multiple scattering and interaction with the free surface.*

3.4.4 Seismometer Output

The other form of output which can be analyzed for quantification or visualization is binned seismic energy. Radiative3D allows for the placement of virtual seismometers along any surface designated as a collection surface. Whenever a phonon interacts with a collection surface within a specified gather radius of a seismometer, the energy of that phonon is collected by the seismometer, decomposed into three cartesian energy axes, and binned into time windows. At the end of simulation, these energy bins are output and can be interpreted as seismic energy traces, suitable for making envelope plots. Figure 4 shows two seismic envelope plots produced by the Radiative3D code. The traces represent 2.0 Hz phonon energy arriving at a virtual seismometer approximately 800 km from a hypothesized earthquake source (left) and explosion source (right) synthesized in a 3-D model of the Lop Nor region having a simple deterministic and trial statistical structure. We set the depth of the explosion event to 2.0 km below the surface, and the depth of the earthquake event to 42.0 km below the surface, comparable to some of the larger magnitude earthquakes to recorded in the Lop Nor region.

Traces from multiple seismometers arranged in a linear array can be combined to make travel-time curves. Figure 5 shows two travel-time curves produces by Radiative3D. The curves represent 2.0 Hz phonon energy from earthquake and explosion sources in a Lop Nor model with complexity near the Moho interface and a velocity ramp just underneath it, resulting in phase arrivals with Pn and Sn timing characteristics.

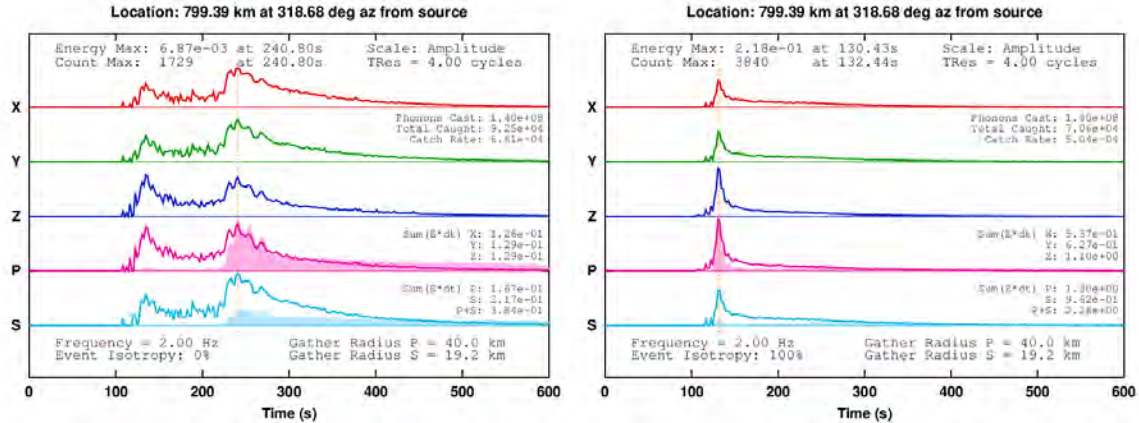


Figure 4. Example coda envelopes for earthquakes and explosions synthesized by radiative transport. *Seismic envelope plots produced by the Radiative3D code for a shallow-focus earthquake (left) and explosion (right). Traces are shown for components of motion NS (Y), EW (X), and vertical (Z) and wave type (P or S) arriving at the receiver. Shaded area under P and S curves represents phonon capture count and serves a diagnostic purpose.*

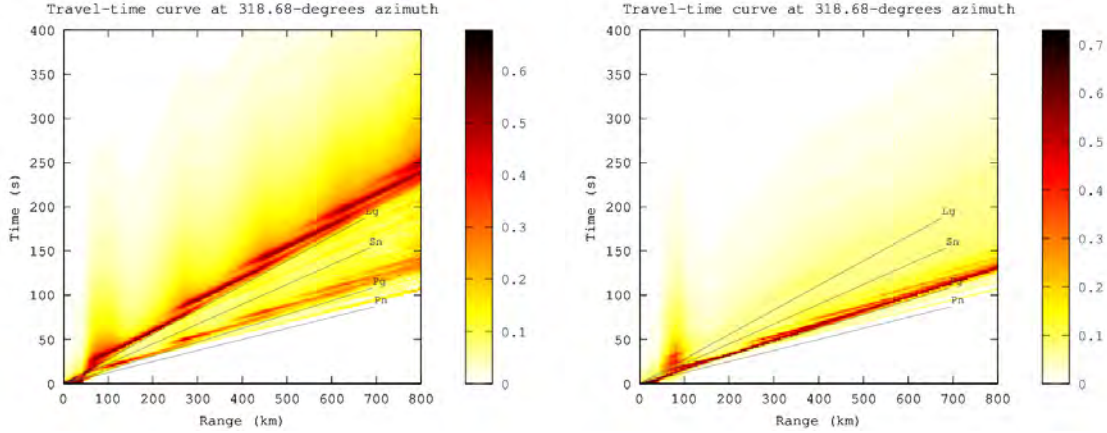


Figure 5. Example coda envelopes displayed as travel time versus distance plots. *Travel time curves produced by the Radiative3D code for a shallow focus earthquake (left) and explosion (right). Image density indicates total energy arriving on all three axes, and makes various seismic phases easily discernable. Left: Earthquake source. Right: Explosion source.*

3.4.5 Features Complete:

Layered multi-cell Earth models:

While full-3D Earth models based on tetrahedral model cells are not yet supported, an intermediate cell type based on stacked cylinders is supported and functional for simulating layered-Earth models. Partial-3D functionality is available because the interfaces between adjacent cylinders can be given an arbitrary inclination. This means that first-order lateral variations, such as a sloped Moho can be modeled.

Reflection/Transmission scattering at discontinuity interfaces:

Free-surface reflections, as well as sharp velocity discontinuities (such as at the Moho layer), require special treatment of ray propagation. Much like the radiation patterns of scattering from small-scale volumetric inhomogeneities, a ray's interaction with an interface across which seismic velocities and/or material densities abruptly change can be thought of as a form of scattering radiation pattern. For a given incident ray, there are up to four different outgoing ray directions, and two different ray types (P and S), with special care being necessary to correctly transform the S-polarization angle. Aki and Richards (1980) develop a set of 20 scattering coefficients that cover all possibilities between incoming P and S waves and their associated transmitted or reflected P or S outgoing waves. These coefficients quantify the amplitude and phase of the outgoing waves, which is used by Radiative3D to compute probabilities of an incoming ray transforming into the corresponding outgoing ray type. This allows for the modeling of reflection (at a free surface or interface) and transmission (interface) of rays with corresponding possibility of transformation between P and S polarization types. This feature has been recently completed in the Radiative3D codebase.

3.4.6 Features in Development

Software development is ongoing, and while we have reached a state where certain studies of real-world significance can be undertaken with the code as-is, there still remain some features being tested before we reach full target functionality. The most significant of these are:

Tetrahedral Model Cells:

Three-dimensional Earth models, having fully general spatial gradients of velocity and density within layers need to be discretized in some fashion. The method we have chosen is to divide the model into tetrahedral cells inside of which the Earth parameters are analytically specified. A tetrahedron is the polyhedron with the minimum number of vertices needed to specify a three-dimensional volume, which allows for straightforward approaches to dividing space into cellular components. Another advantage of tetrahedra, (over, e.g., rectangular prisms), is that Earth parameters specified on the four vertices allows unique and complete specification of the properties in terms of linear gradients throughout the volume of the cell.

Much of the infrastructure for cellular model discretization is already complete in the code, and is utilized in the layer-celled structure already supported in the code. Implementing cells with tetrahedral geometry remains primarily an implementation detail at this point.

Velocity Gradients:

In a uniform-velocity medium, ray paths are straight lines. In the real Earth, rays can follow curvilinear paths. The plan for Radiative3D is for velocities to be specified as first-order gradients, resulting in paths which are circular arcs within a given model cell. This allows for a much more natural representation of real Earth structure, and lessens the detail needed to represent that structure. At present Radiative3D supports only uniform velocities (gradients on the macro level can be represented as a multicellular stair-step model). The next development step of Radiative3D will be to implement support for velocity gradients. This step will naturally follow the implementation of tetrahedral model cells, since this geometry allows the unique specification of the gradients by specifying known velocities on the cell vertices.

Anisotropy of Heterogeneity Scale Lengths

Anisotropy of heterogeneity scale lengths that scatter high frequency seismic waves can affect coda shapes (Hong and Wu, 2005) and spatial coherence of amplitudes (Tkalcic et al., 2010) depending on the angle their wavefronts make with the axes of vertically or horizontally stretched heterogeneity. Nielsen and Thybo (2006), for example, found the need to incorporate horizontally stretched heterogeneity to model Pn and Sn codas observed in Russian PNE data. We have made some tests for the effects of

the radiation patterns of vertically or horizontally stretched heterogeneity (Cormier et al., 2011). A more efficient simulation of the effects of heterogeneity stretched in a quasi-horizontal direction might be to simply combine random perturbations to thin layering together with isotropic heterogeneity. This can be accomplished with our existing code.

3.4.7 Features Not Currently Targeted:

In addition to the code features detailed above, another feature, not currently targetted for development, remains within feasible reach of the codebase as it now stands, and may provide a starting point for future work. In particular, while Radiative3D currently produces seismic envelope plots, it is technically possible to produce full-waveform seismograms by tracking not only the amplitude, but also the phase, of each phonon as it propagates through the model. By binning the seismic energy as amplitude phasors rather than energy scalars, full seismograms, rather than envelopes, can be produced. Phase tracking through direct propagation is trivial, as it is proportional to the product of frequency and travel time. Slightly more intricate are the phase shifts that result from scattering events, and from reflection/transmission interactions with discontinuity or free-surface interfaces. These phase factors, however, are actually already calculated by the codebase when it calculates scattering and reflection/transmission probabilities. Adding the accounting necessary to track cumulative phase through a phonon lifetime would be a very tractable problem.

4. RESULTS AND DISCUSSION

4.1 Lop Nor Region: Deterministic Model and Data

We focused our modeling efforts on the Lop Nor, China region (Figure 6) because of it is one of few regions in which nuclear tests and earthquake waveforms are well recorded at accessible global seismic stations and networks. Sykes and Nettles (2009) found that more than half of the earthquakes in the Reviewed Event Bulletin (REB) of the IMS that occurred within 100 km of six Lop Nor test sites from 2000 through 2008. LANL has also constructed maps of regional wave propagation efficiencies in this region (Phillips et al., 1999). Lop Nor is located near the southeastern side of the Tien Shan, a region of moderate earthquake activity and contemporary horizontal compressive stress in the earth's crust, which can be an important factors in inducing tectonic release from underground nuclear tests in this region.

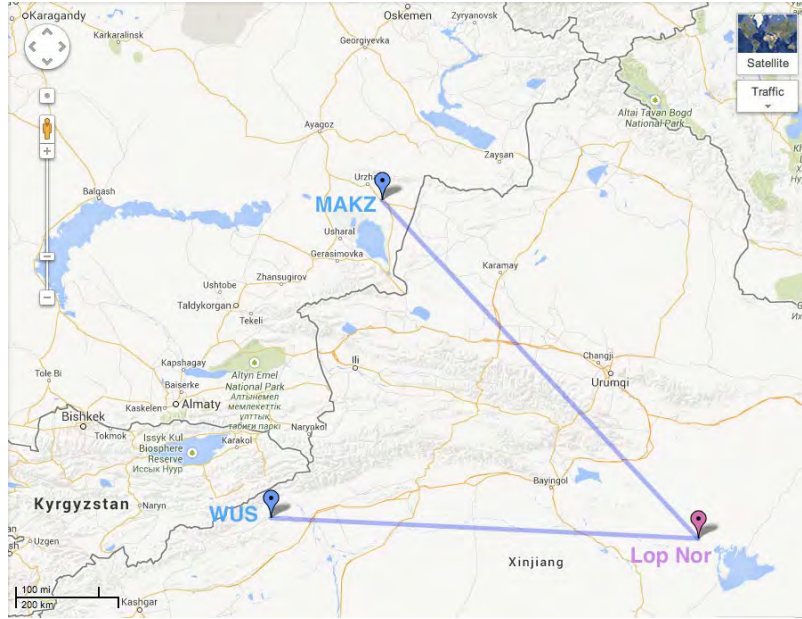


Figure 6. Lop Nor test site region and paths to seismic stations MAK and WUS. *Lop Nor test site and paths to regional seismic stations MAK and WUS on which we have concentrated modeling tests.*

The Chinese station Urumqi (assigned the station code WMQ by seismologists) is about 2.15° (250 km) from Lop Nor. Stations MAK and WUS are $\sim 6.85^\circ$ from Lop Nor. For the earthquake and explosion data we use seismograms from events downloaded from IRIS-DMC.

Figure 7 shows some waveform examples from the Lop Nor region. The data come from an explosion at the Lop Nor site as recorded at station MAK at great circle distance 6.85° and an earthquake in the same area recorded at both MAK and WUS. WUS is approximately at the same distance from Lop Nor as MAK but in at different azimuth. The left column in Figure 7 shows the data bandpassed between 1-2 Hz and the right column shows a bandpass between 6-8 Hz. Not only are there differences between the earthquake and explosion data at MAK, there are also differences between the earthquake traces at MAK and WUS in the time windows commonly used to measure Pn/Lg and Pg/Lg amplitude ratios.

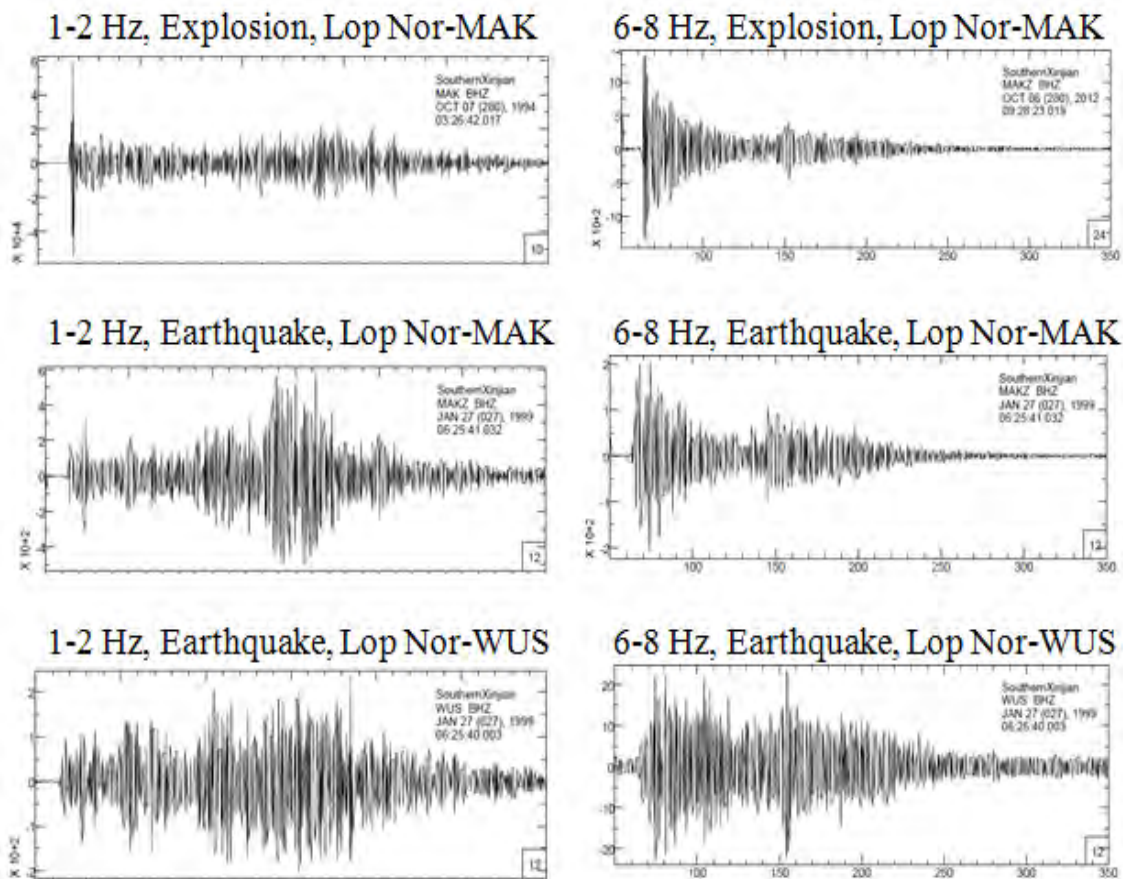


Figure 7. Vertical component bandpassed data recorded at WUS and MAK from the Lop Nor region.

Using known elevations of Lop Nor and seismic stations MAK and WUS, along with Moho depths from the Cornell Moho model (atlas.geo.cornell.edu/geoid/imagegrid.html) and layer profiles from CRUST 2.0 (Laske et al., 2011) at those same locations, we located and oriented a set of five crust layers (sediments, upper, middle, and lower crust, and top layer of the mantle). Additionally, we defined an additional 16 mantle layers from AK-135-F (Kennett et al., 1995) and regionalized perturbations (Gudmundson and Sambridge, 1998) to a depth of 859 km. These layers served as a model in which to run early test synthetics.

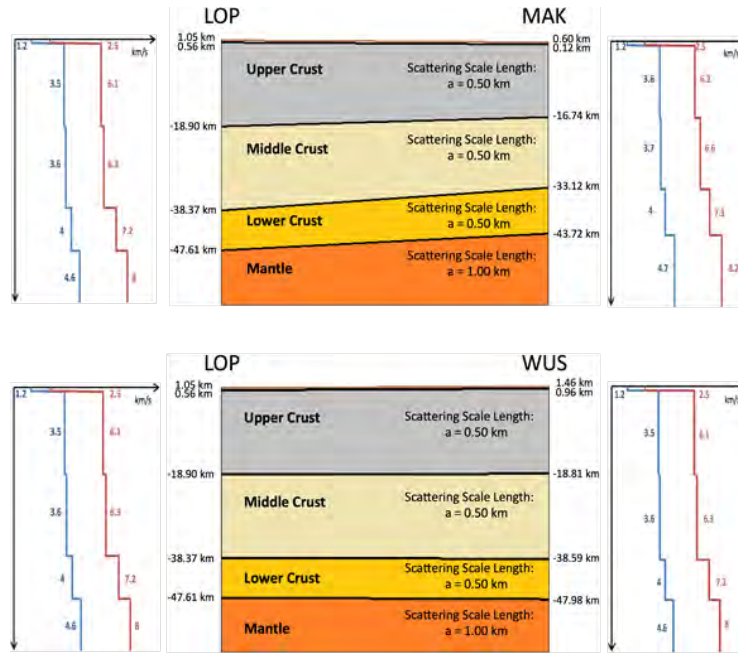


Figure 8. Simplified Lop Nor region earth model. *A thin sediment layer is included.*

4.2 Sensitivity of Coda Envelopes to Statistical Parameters

Since there are no documented, large-scale, differences in crustal thicknesses between the paths to MAK and WUS, and we could not find any previous work that has connected observed coda with parameters describing a heterogeneity spectrum, we have performed a series of experiments to examine the sensitivity of regional phases, in general, to parameters that describe the small-scale statistical structure. All tests of the effects of statistical parameters have employed the von Karman power spectral density function (PSDF) (Figure 1). The advantage of this spectrum is that it can incorporate changes in slope of the power spectrum over a broad band of wavenumbers, typical of media having a fractal-like behavior of scale lengths, as well as a corner wavenumber above which the power spectrum more strongly decays, consistent with either the existence of a limiting small scale or a limiting sensitivity of the wavefield at frequencies outside the pass band of a filtered seismogram. The parameters varied are the fractional fluctuation ε of wave velocities, ($\varepsilon = \frac{\Delta V_P}{V_P} = \frac{\Delta V_S}{V_S}$), and a parameter ν controlling the density perturbation as factor multiplying the P velocity fluctuation, a scale length a that controls the wavenumber corner, and a von Karman order number κ that controls the slope of the power spectrum after its corner.

We investigated the sensitivity of regional phase codas to heterogeneity parameters using two methods: (a) calculation of the mean free path (MFP) and the dipole projection (DP) while varying each of the parameters and holding the others constant and (b) simulations of earthquakes and explosions at a number of frequencies and a variety of parameters.

The MFP and DP calculations provided a fairly quick and accurate way to understand the general effects of the parameters. The MFP reports how far a phonon will travel (in km) before it encounters a scattering event. Longer MFPs mean less scattering. The dipole projection gives information about the direction the phonon takes after it is scattered and varies from -1 to 1. A value of 1 means it is 100% likely to continue in its forward direction, and a value of -1 means it is 100% likely to be totally scattered backwards.

In figures plotting the effects of varying a parameter, MFP is plotted on the left side y -axis and shown as solid lines, while DP is plotted on the right side y -axis and shown as dashed lines, and the parameter being varied is plotted on the x -axis. The red lines show the effect of scattering on the P-wave phonons, and the blue lines show S-wave phonons. For all parameter variations, synthetic envelopes are computed at 2 Hz. The effects of varying each heterogeneity parameter on the synthetic envelopes for earthquakes and explosions are compared to the effects of a reference set of parameters (Table 1). Q_p is assumed to be greater than Q_s by a factor of approximately 9/4, consistent with an assumption of viscoelastic attenuation purely in shear and a Poisson's ratio of $\frac{1}{4}$ (e.g., Anderson, 1989). Figure 9 shows the synthetic envelope for the reference parameters listed in Table 1 with some of the features labeled. For comparison with our mantle values, Hedlin, et al. (1997) report the P velocity perturbation throughout the mantle as approximately 1% and for a equal to 8 km. The frequency band of their teleseismic data, however, is not sensitive to the smaller scale length a required needed to model the coda of regional higher frequency data.

Table 1. Reference heterogeneity parameters used for synthetic comparisons.

	nu	eps	a	kappa	Qs
Sediments	0.8	0.01	0.25	0.2	50
Crust	0.8	0.04	0.2	0.3	1000
Mantle	0.8	0.008	0.2	0.5	300

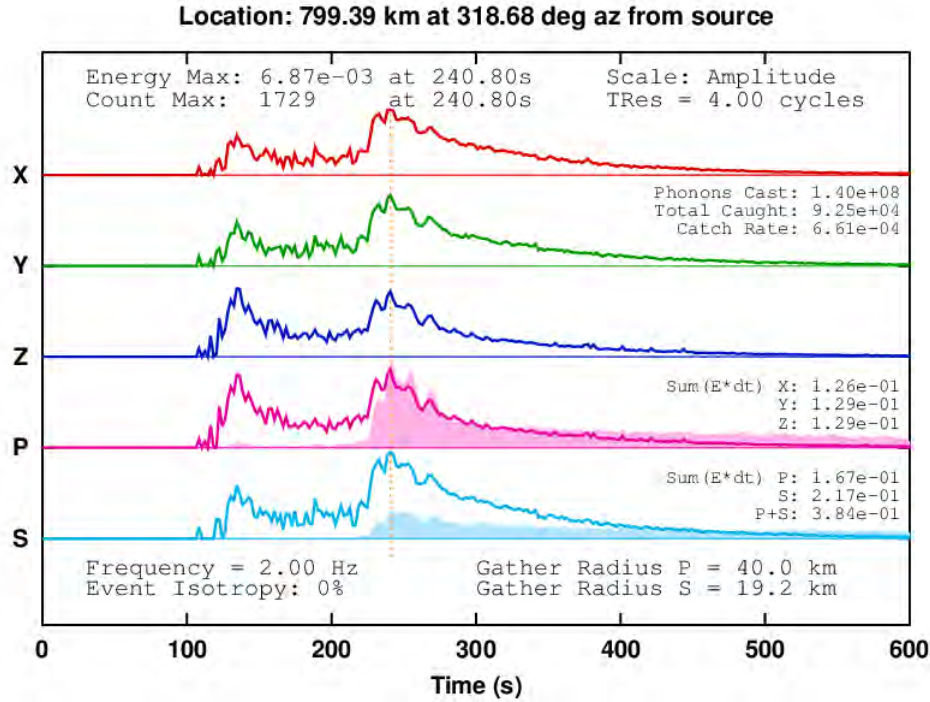


Figure 9. Coda envelope synthetics for earthquakes in the Lop Nor region for a reference heterogeneity spectrum. The vertical dotted red line gives the location in time of the energy maximum, which is also listed at the top of the figure. The bottom left corner of the figure includes the frequency of the run (in this case 2 Hz) and the isotropy of the moment tensor representation of the source (0% indicates earthquakes and 100% indicates explosions). Phonon statistics listed on the right side of the figure include the total number of phonons cast during this simulation (in this case 140 million), the total phonons caught at this location, and the catch rate. Also listed on the right side is the sum of the energy captured. The total energy is indicated as P+S.

4.2.1 Magnitude of Velocity Perturbation ϵ

Figure 10 shows the effects of velocity perturbations on MFP and DP. The dashed lines reflect a constant S-wave dipole projection of 0.48 and a constant P-wave dipole projection of 0.18. Varying epsilon has no effect on the scattered phonon's preferred direction of travel after scattering because the magnitude of epsilon does not affect the shape of the scattering radiation pattern at a scattering event. On the other hand, there is an apparent exponential decrease in the MFP for both P and S phonons for this range of velocity perturbations. We should expect to see increased coda production for both S and P waves in the synthetic envelopes with increased epsilon.

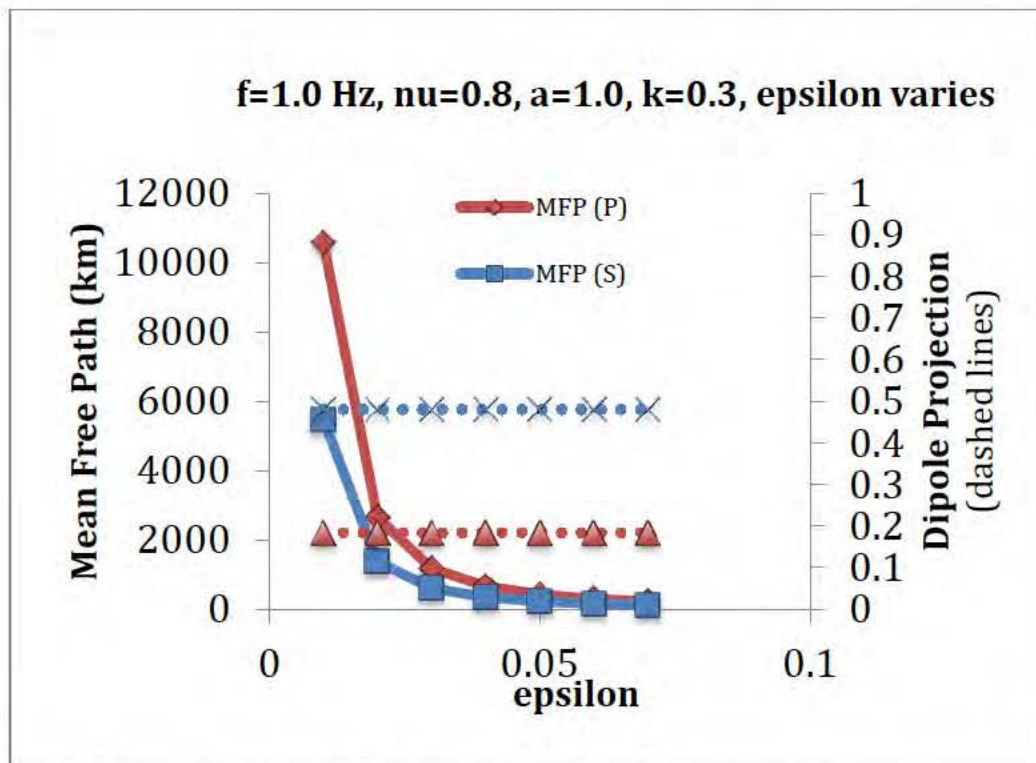


Figure 10. Mean free path and dipole projection for velocity perturbations

Figures 11a,b compare a high velocity variation (epsilon) in the crust to the Reference synthetic envelopes (0.08 vs. 0.04) for a frequency of 2 Hz. For the earthquake, the maximum energy and maximum phonon count in the Reference are both associated with the Lg phase (occurring at ~ 241 s). For the explosion, the maximum energy and maximum phonon count in the Reference are both associated with the P coda (occurring at ~ 130 s). We see a number of effects in the seismic envelopes caused by the change in the heterogeneity parameter, including change in total energy and phonons arriving at the receiver, change in maximum energy (giving an indication of phase amplitude), onset of P and Lg phases, shape of direct phase arrival (pulse), and coda following the direct arrival.

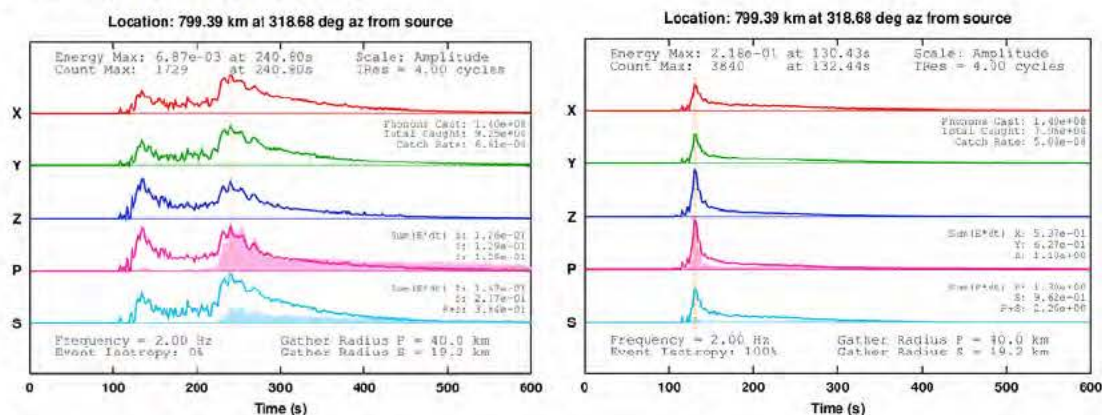


Figure 11a. Earthquake (left) and explosion (right) coda envelopes for low epsilon.

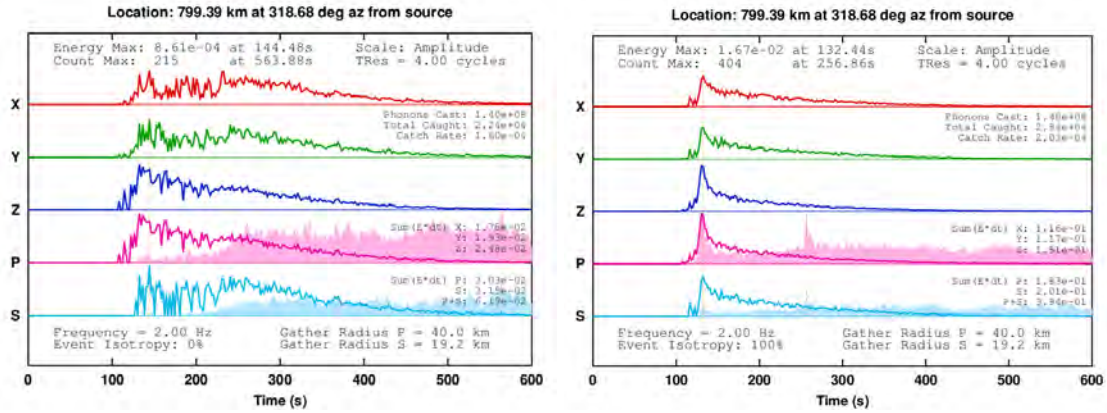


Figure 11b. Earthquake (left) and explosion (right) coda envelopes for high epsilon.

The combined results of the MFP/DP plots and synthetic envelopes show that with higher velocity perturbations, the phonons have smaller mean free paths, thus encountering more scattering events. The lack of change in the dipole polarization, however, demonstrates that energy tends to scatter more towards the direction of the paths before the scattering events, and will eventually reach their original destination. The shift in arrival time of the maximum energy in the earthquake envelope from the Lg arrival window to the P arrival window reflects the fact that S-waves are more sensitive to velocity fluctuations than P waves.

The scattering caused by the increase in the velocity perturbation produces a marked redistribution in energy, stretching it out over a longer period of time. This is represented by a slower decay of coda envelopes, the broadening of the pulses, and a pronounced delay in the phonon arrivals (shaded area). These results reflect the increased production of scattered P and S energy as well as conversions between P and S energy (particularly for the explosion). Without scattering, almost all of the explosion energy is in the P arrival. With the scattering, in addition to coda energy following the P-arrival, there is significant energy arriving at the time we would expect to see Lg. This delayed energy, however, is reflected in a slower coda envelope decay following the P phases, which cannot easily be mistaken for the typical Lg coda envelope observed from earthquakes. This strongly suggests that mechanisms other than scattering alone need to be considered to explain observations of anomalous low Pg/Lg ratios from some explosions.

4.2.2 Magnitude of Density Perturbation ν

The density perturbation is a multiplier of the velocity perturbation: $\frac{\Delta\rho}{\rho} = \nu \frac{\Delta V_P}{V_P}$.

Figure 12 shows the effects of density perturbations from 0.3 to 1.5 on MFP and DP. Higher values of ν produce a shorter mean free path as expected. In contrast to the effect of increasing velocity variations, the effect of increasing density variations is a linear rather than the exponential decrease in mean free path. The higher values of ν also lower the dipole projection, which means the phonons are scattered further away from the forward direction of travel. This suggests that ν variations will be important in

controlling the attenuation of the peak amplitudes of regional phases defined from narrow windows of group velocity.

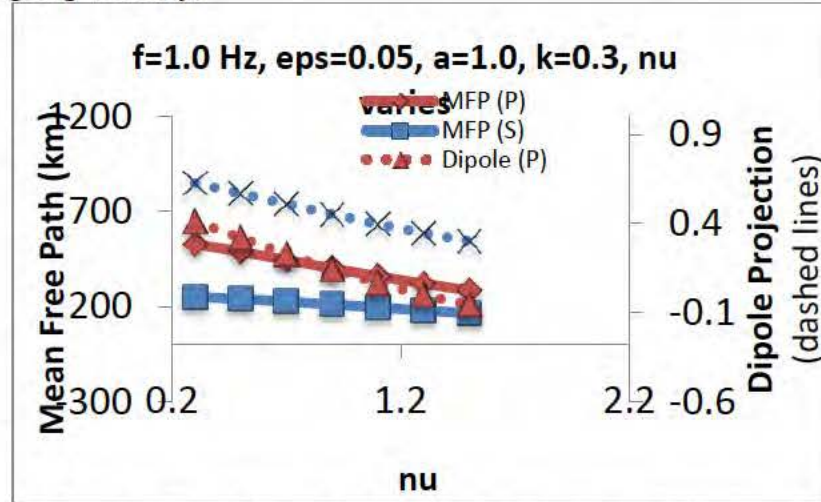


Figure 12. Mean free path and dipole projection for density perturbations.

Figure 13 compares a high density perturbation to the Reference synthetic envelopes (1.6 vs. 0.8 in the crust). The maximum energy occurs at the same time as the Reference, and the maximum phonon count occurs only slightly later (~ 255 s). The P onset appears to be sharper. There is a lower amplitude as some of the energy arrival is delayed, but the effect is not as pronounced as that of the velocity perturbation.

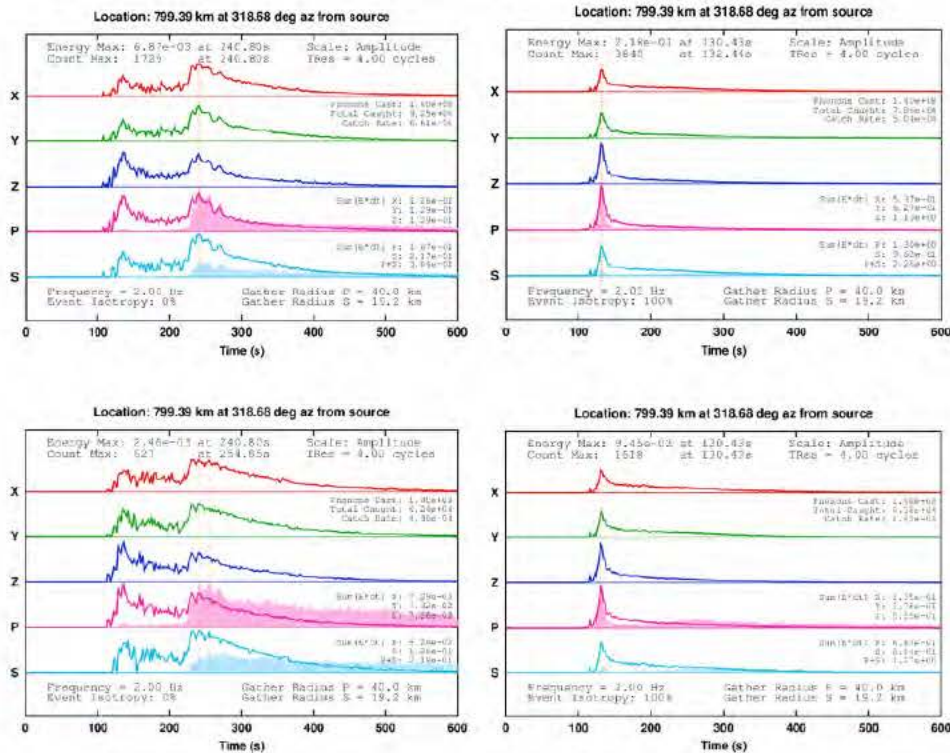


Figure 13 Synthetic coda envelopes for density perturbations. *Top: Reference earthquake (left) and explosion (right). Bottom: effects of increased density perturbation.*

In general, the influence of density variations is to produce more scattered energy than for velocity variations alone. The ability to adjust ν could be important in other seismic coda studies, such as those involving partial melt (Hong, et al., 2004). Shearer and Earle (2008) take ν 0.8 for small-scale heterogeneity (1-10 km). For larger scale structure in the mantle, geodynamicists take ν on the order of 0.2 or less because large values cannot be sustained by buoyancy.

4.2.3 Scale length a

Figure 14 shows the effects of scale length variations from 0.5 to 12 km on MFP and DP. For the velocities and frequency (2 Hz) used in coda envelope simulations, the wavelength in the crust is 2 km for the S waves and 3.4 km for P waves.

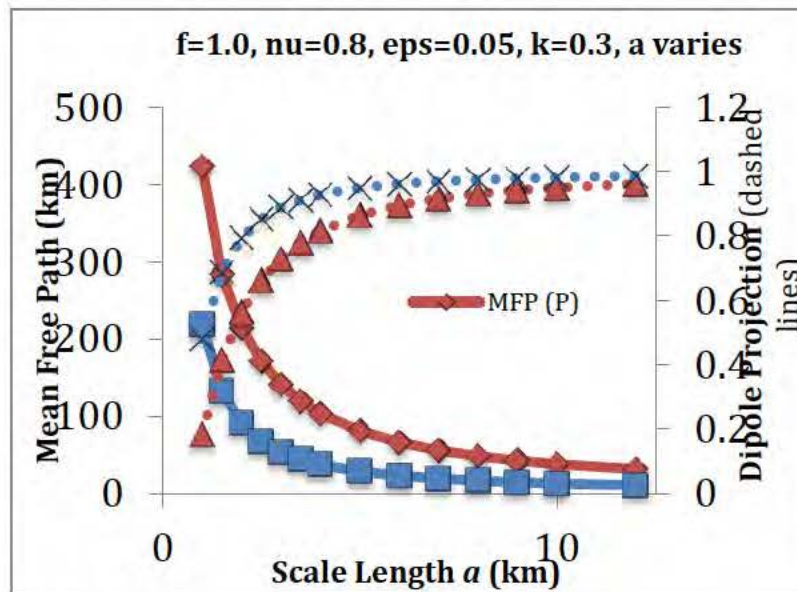


Figure 14. Mean free path and dipole projection for variable scale lengths of a von Karman spectrum.

Figure 15 shows synthetic envelopes for three changes in the scale length: doubled compared to the Reference (0.4 km), 3 km, and 12 km. This allowed us to examine the effects of the scale length being greater than the wavelength. The mean free path exponentially decreases as the scale length approaches the wavelength, but the dipole projection exponentially increases toward 1 (forward scattering). Not surprisingly, the competition between these two effects results in the changes the shape and attenuation of regional phase codas most strongly when the scale length is on the order of the wavelength, near the intersection of the MFP and DP curves in Figure 13.

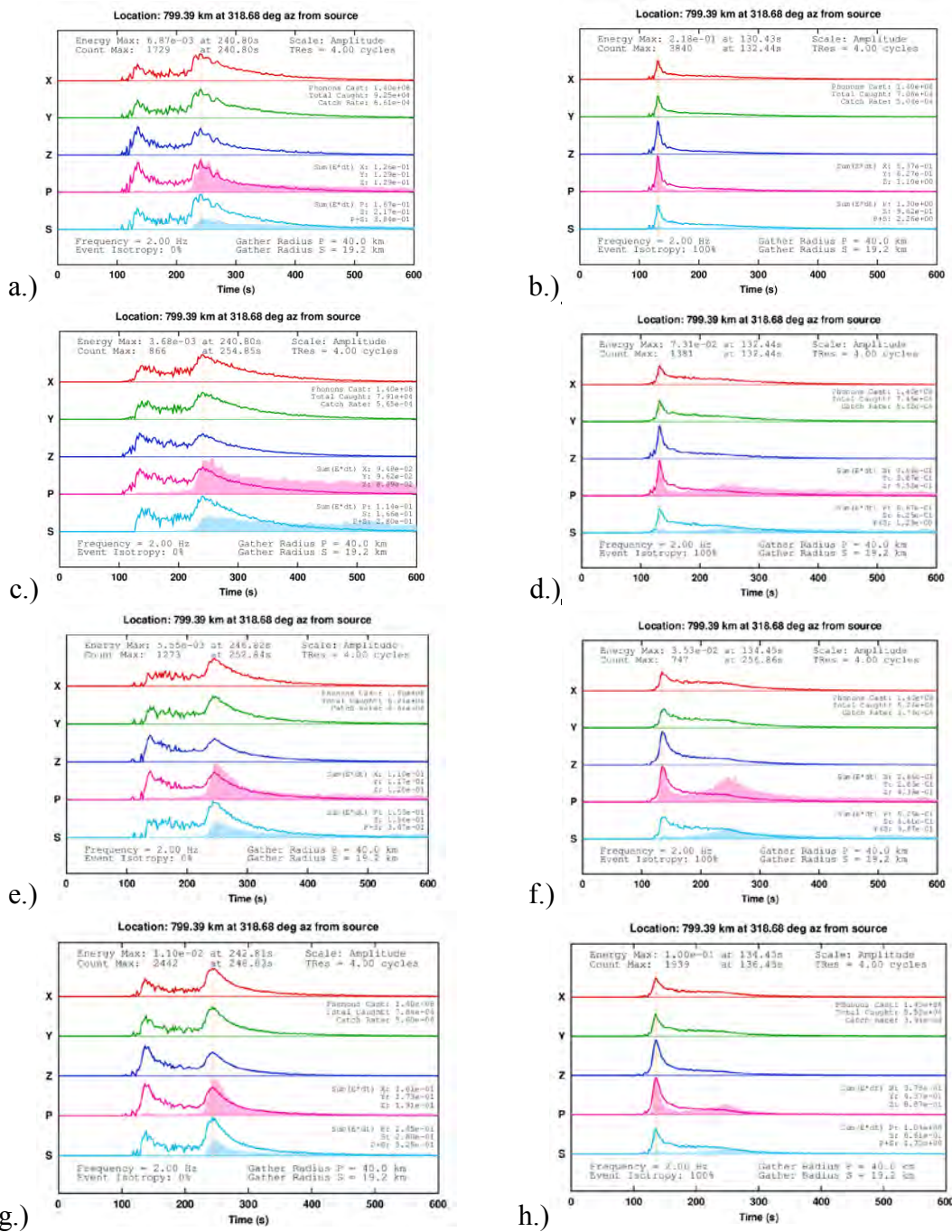


Figure 15. Synthetic coda envelopes for variable scale lengths of a von Karman spectrum. (a.) earthquake Reference, b.) explosion Reference, c.) earthquake 0.4 km scale length, d.) explosion 0.4 km scale length, e.) earthquake 3 km scale length, f.) explosion 3 km scale length, g.) earthquake 12 km scale length, h.) explosion 12 km scale length).

4.2.4 Hurst Parameter κ

The fluctuation spectra for the von Karman medium are flat up to a corner wave number inversely proportional to the correlation distance and then fall off at higher wave numbers ($ka > 1$). It is also characterized by heterogeneities that are self-similar for $ka > 1$. This medium is "rougher" at small length scales than the exponential medium (Frankel and Clayton, 1986).

Figure 16 shows the effects of κ variations from 0.1 to 0.8 on MFP and DP. As kappa increases, the MFP decreases, which cause scattering delays in the energy arrival. As the slope of the heterogeneity spectrum flattens above the corner wavenumber the scattering is increasingly in the forward direction even though scattering events are more frequent. The effect of increased scattering at higher kappa will have less effect on redistributing energy and stretching coda envelopes but may have a stronger effect on equilibrating energy on the three components of motion due to a more frequent sampling of the heterogeneity radiation patterns that control polarization and wave type (P or S). The heterogeneity power, however, will decrease faster at wavenumbers above the corner wavenumber for higher kappa. Thus the effect of different κ 's can be expected to be minor, which we found to be true in our experiments with synthetic coda. Since visible effects are not easily discernible, we do not show synthetics for this experiment.

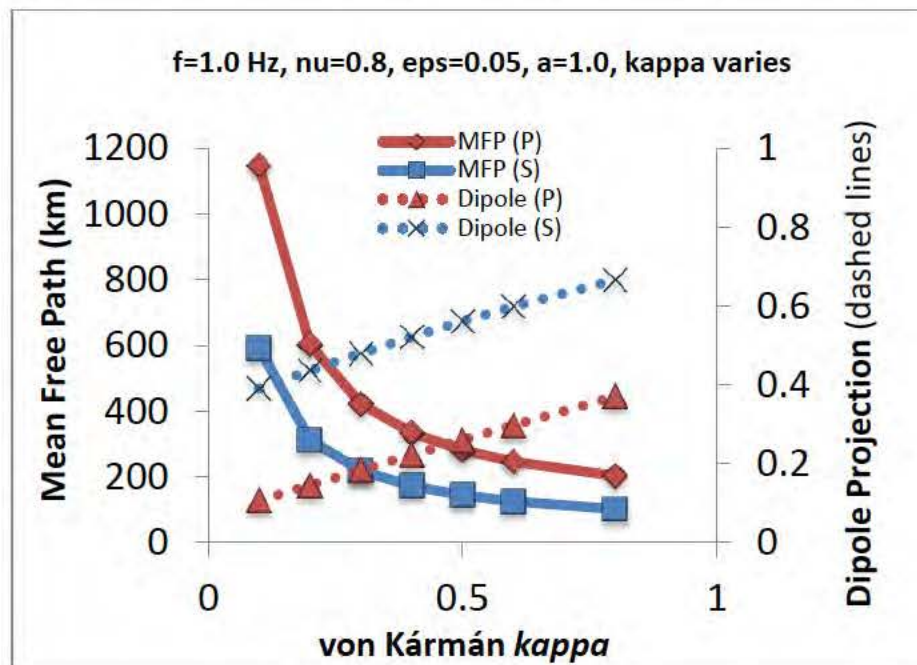


Figure 16. Mean free path and dipole projection for the Hurst parameter κ , which controls spectral shape for wavelengths larger than the scale length of a von Karman spectrum.

4.3 Intrinsic Q Effects

Radiative3D allows us to treat intrinsic, viscoelastic attenuation separately from scattering to help determine their relative contributions to the total attenuation of peak coda amplitudes or to separate their contributions to measured coda-Q's. Figure 17 compares coda envelopes against the synthetic envelopes for the Reference deterministic and statistical model of heterogeneity with and without intrinsic attenuation. For the earthquake, the 2 Hz. total energy without Q^{-1} included is about 100 times that of the reference envelope with the maximum energy value about 50 times that of the reference. The phonon capture is about the same. The effect of Q^{-1} is to reduce the amount of energy in each phonon as a function of time traveled. For the explosion, the 2 Hz total energy, without Q^{-1} included, is about 10 times that of the reference synthetics, with the maximum energy value about twice that of the reference. The phonon capture is about the same.

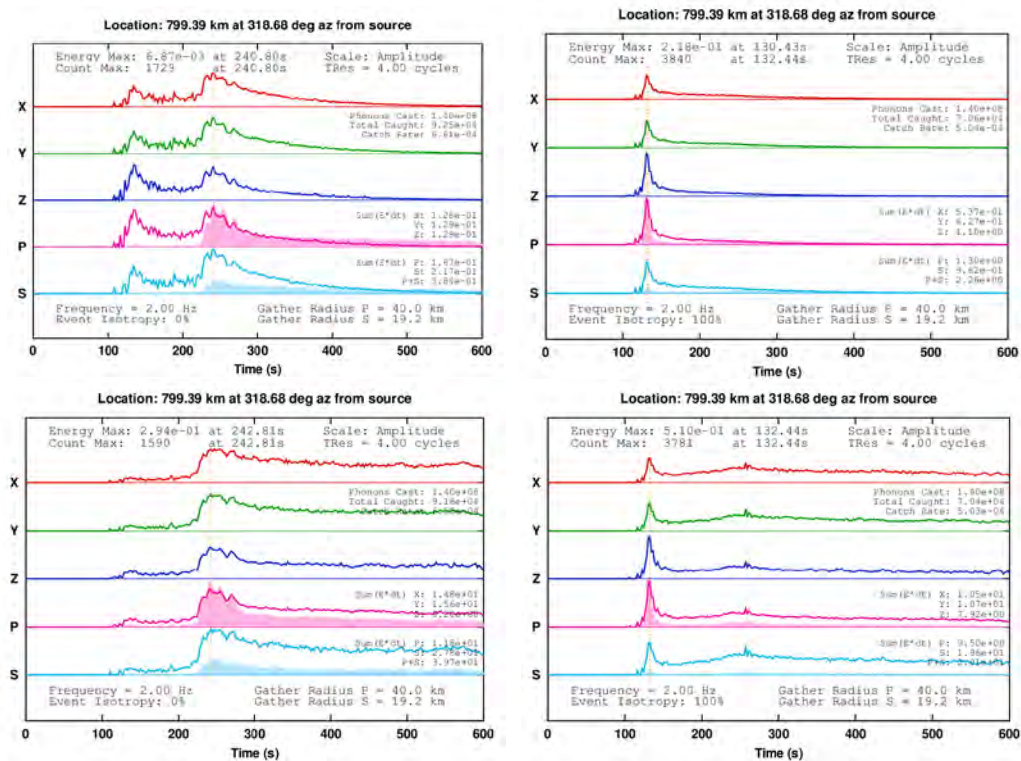


Figure 17. Synthetic coda envelopes for earthquakes and explosions with and without intrinsic attenuation. *Top left: earthquake reference; top right: explosion reference; bottom left: earthquake without intrinsic attenuation; bottom right explosion without intrinsic attenuation.*

This test shows that not adding intrinsic attenuation results in the coda energy being unrealistically extended in time. Future work with the radiative transport algorithm will allow the parameter space of scattering intrinsic attenuation to be fully explored to examine tradeoffs that can produce a fit to regional coda shapes. Accurate models of intrinsic Q in the crust and just beneath the Moho are essential for proper modeling of Sn and Lg.

4.4 Surface layer effects

A highly heterogeneous, strongly scattering, sediment layer may affect regional phase coda (Baumgardt, 2001), particularly for shallow emplaced explosions. Figure 18 shows example synthetic envelopes exploring the effects of a 0.5 km thick sediments layer with the velocities, density, and Q 's given in Table 2. The first row of the envelopes are the Reference synthetics from the heterogeneity parameter study. In the second row of envelopes the velocities in the sediments layer have been adjusted to nearly match those of the crust layer immediately below. The thin layer in which low velocities have been inactivated is still treated separately for scattering, although for this test is epsilon equal to 0.04, matching the values used in the thicker crustal layer.

Table 2. Deterministic properties of test sediment layer.

	V_P	V_S	Density	Q_P	Q_S
Sedi Layer	2.50	1.20	2.10	162.8	50.0
Upper Crust Layer	6.13	3.53	2.75	2261.7	1000.0

For both the earthquake and the explosion, the most obvious result of the low velocity sediment layer is on the P/Lg amplitude ratio. Although the differences between earthquake and explosion envelopes are strong in both cases, the effect of the sediment layer will be to slightly reduce the effectiveness of the P/Lg discriminant. The instantaneous state of scattered phonons arriving at the receiver will be more equal in P and S for the case of the sediment layer. This is also apparent in the tendency of the sediment scattering layer to equilibrate energy on all three components of motion (X, Y, Z).

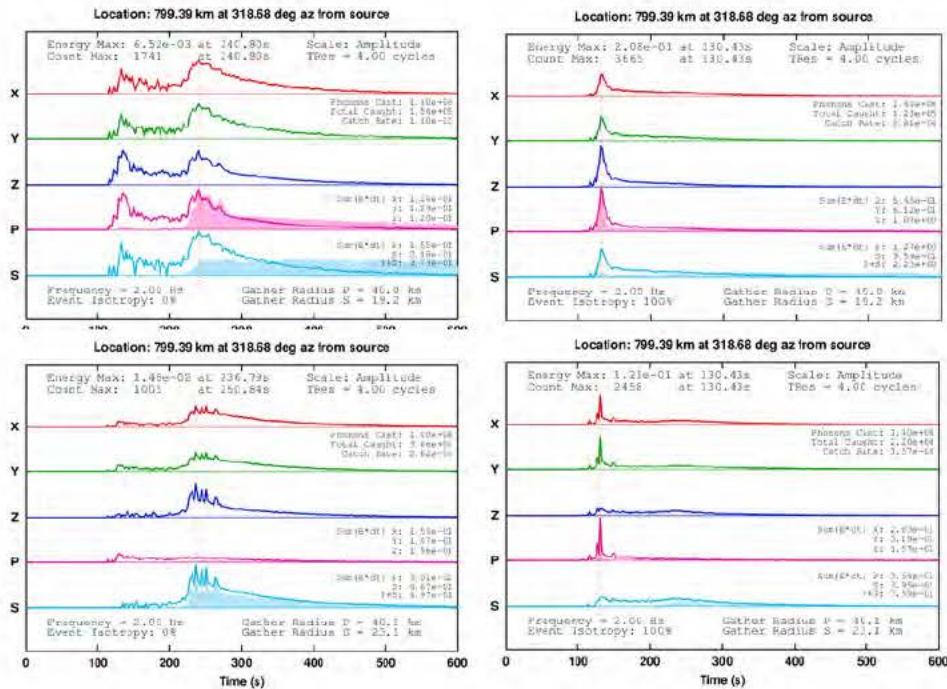


Figure 18. Synthetic coda envelopes for earthquakes and explosions with and without a thin sediment layer. *Top left: earthquake Reference; top right: explosion Reference; bottom left: earthquake no sediments; bottom right: earthquake no sediments.*

4.5 Pn and Sn

High frequency Pn and Sn are traditionally thought of as head waves traveling just beneath the Moho discontinuity. Early attempts to model high frequency Pn and Sn as classical head waves failed because the amplitude in a classical head decays with frequency as $1/\omega$. These phases are now recognized as interference head waves (Cerveny and Ravindra, 1971), which have a representation as series of body waves that are multiply reflected along the underside for either a Moho following Earth's curvature or for velocities that increase with depth beneath the Moho. Our initial experiments assumed a flat earth and homogeneous layers, separated by at most planar tilted layers. In these models energy could not return from the mantle except as scattered waves. With a series of stair step discontinuities, we have simulated the effects of Earth curvature via an earth-flattening transformation and positive velocity gradients with decreasing radius (Figure 19). These modifications allow Pn and Sn to return to the surface after being multiply reflected by and scattered beneath the Moho. Envelopes were synthesized for the southern Xinjiang earthquake recorded at MAK (Figure 20) for this Moho model. Figure 21 shows the results of this experiment with scattering from the reference statistical model turned on and off. A sharp Pn arrival is visible in Figure 21. Sharp arrivals preceding Lg, which can be interpreted as Sn, are best visible in the envelopes having scattering turned off.

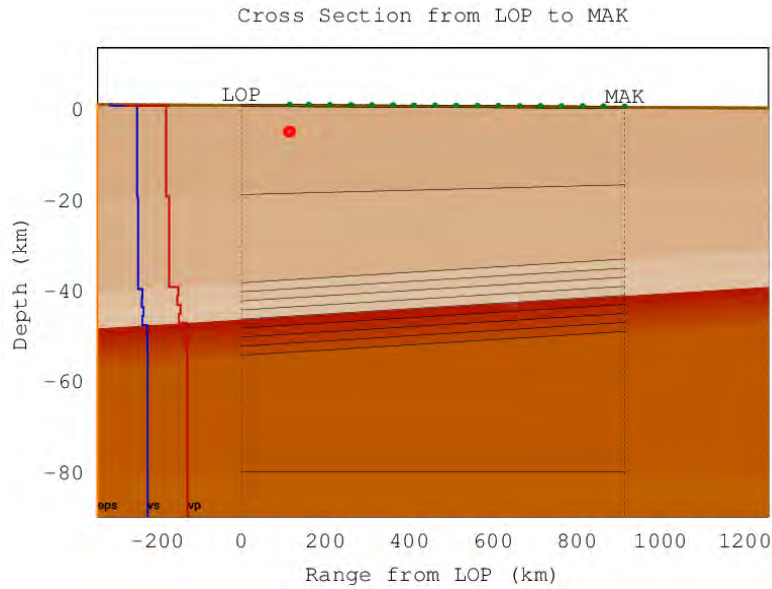


Figure 19. Cross-section of an Earth model having a Moho transition specified by a series of stair-step layers.

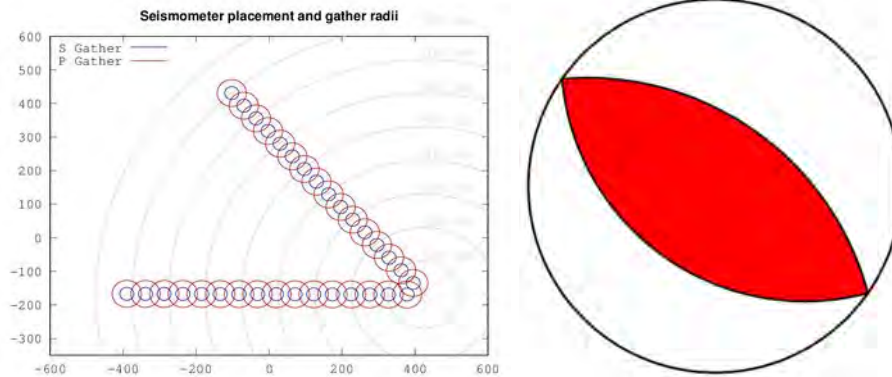


Figure 20. Lop Nor paths to MAK and WUS and source mechanism of a southern Xinjiang earthquake. *Left: receiver placement, phonon gather radii, and epicenter of southern Xinjiang earthquake. Right: mechanism of earthquake.*

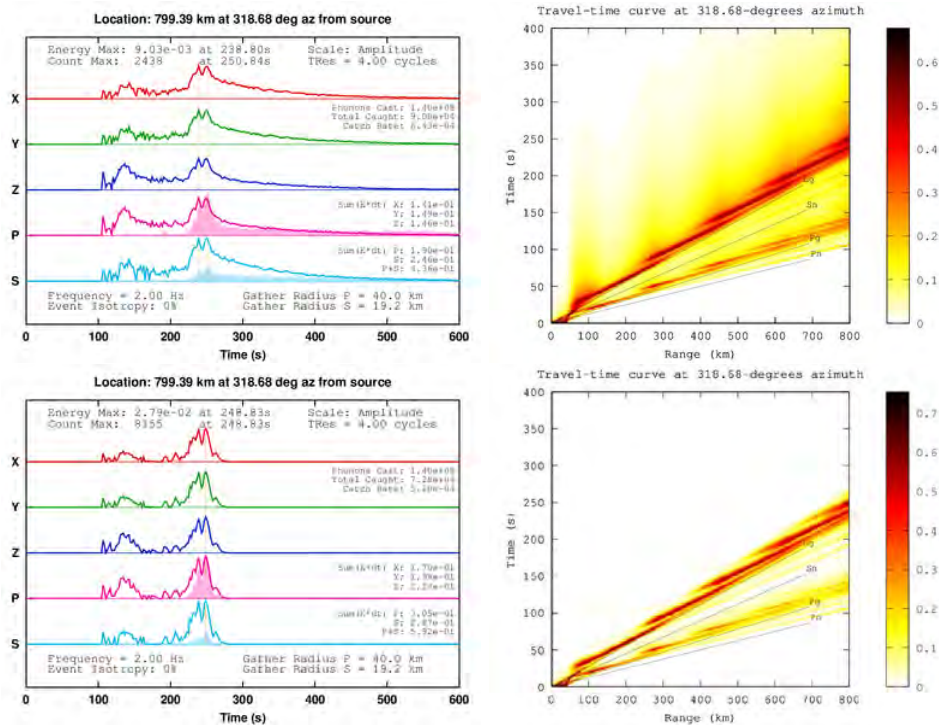


Figure 21. Synthetic coda envelopes for earthquakes and explosions in a Lop Nor model having a Moho transition. *Top: Synthetic envelopes for the Moho transition model for the path to station MAK from the southern Xianjiang earthquake mechanism shown in Figure 22 with scattering predicted from the reference statistical model turned on. Bottom: synthetic envelopes for the same path with scattering turned off.*

Figure 22 compares synthetic envelope against the recorded earthquake. There is good agreement in arrival time and relative amplitude for the Pn, Pg, and Lg phases. The Sn phase is much smaller in the synthetic compared to the data. We believe that reducing the intrinsic S attenuation may allow more of the Sn energy to show up for this phase.

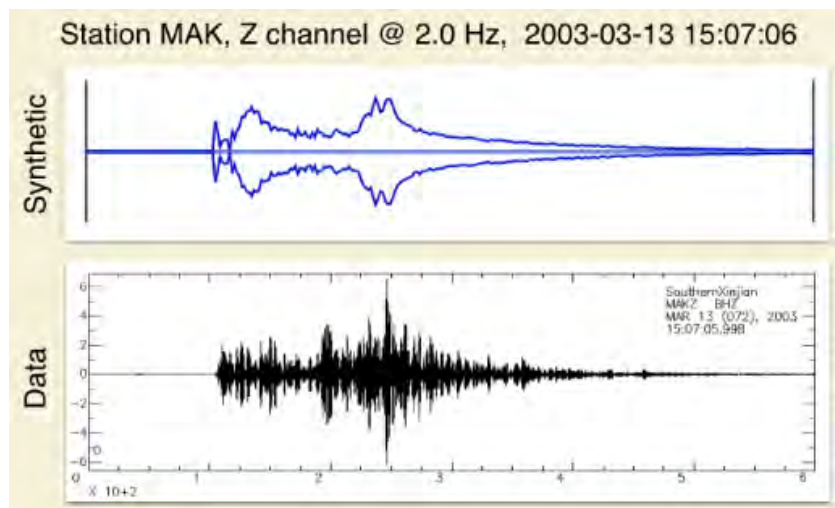


Figure 22. Comparison of 2 Hz synthetics with observed waveforms and passed for 2 Hz. *Comparison of data (below) with synthetic coda envelope (above) for a model having a Moho transition layer.*

4.6 Synthetics compared with data by frequency band

Radiative3D is run at a single frequency and can create simulated seismogram envelopes at any frequency. This allows analysts to interpret the structural or source origin of frequency-specific effects on narrow bandpassed seismic traces. Table 3 lists the values of the parameters used to generate synthetic envelopes that include Pn and Sn phases. These are similar to the Reference parameters used in the heterogeneity parameter sensitivity study with a transition layer added at the Moho as discussed above.

Table 3. Scattering parameters for frequency comparisons.

	nu	eps	a	kappa	Qs
Sediments	0.8	0.01	0.25	0.2	50
Crust	0.8	0.04	0.2	0.3	1000
Transition	0.8	0.008	0.2	0.5	2000
Mantle	0.8	0.008	0.2	0.5	300

There is now a substantial body of empirical evidence that regional P/S ratios provide poor discrimination below some frequency, typically about 2 to 3 Hz, and useful discrimination at higher frequencies, e.g., Fisk 2006. Hence, in Figure 23 we compare computed envelopes against narrow bandpassed data at 2, 3, and 4 Hz.

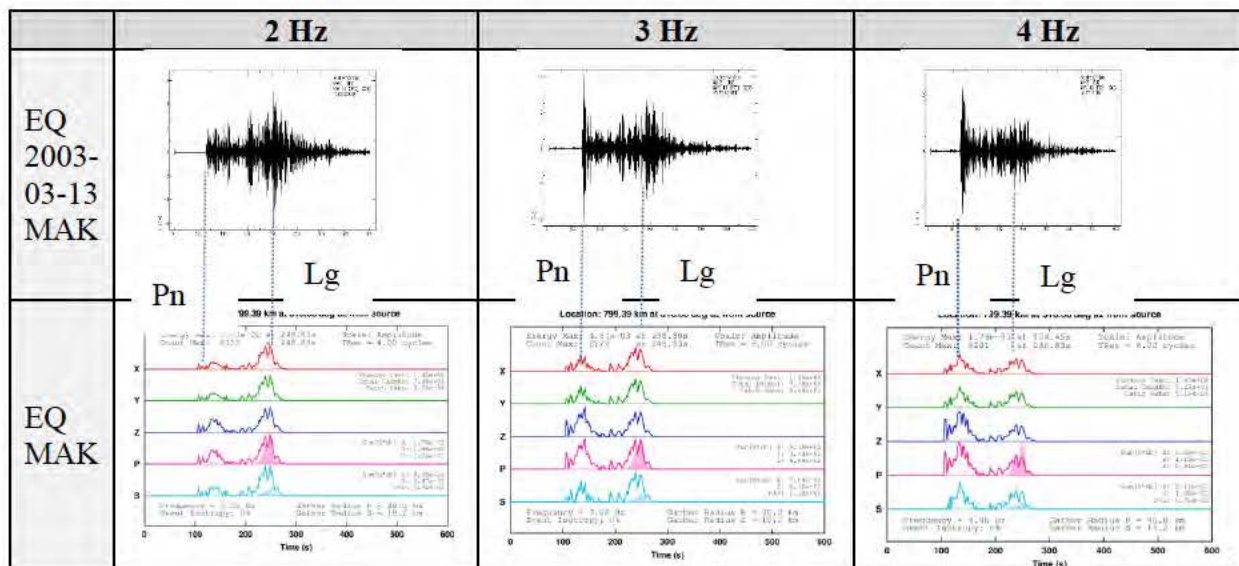


Figure 23. Synthetic coda envelopes compared with data recorded at MAK for a series of frequencies. *Synthetics compared against data recorded at station MAK for the 2003-03-13 earthquake for frequencies 2, 3, and 4 Hz. The approximate arrivals of the regional crustal phases (Pg and Lg) are marked. The relative changes in amplitude of the Pg and Lg phases produced by the synthetics agree quite well with the data.*

4.7 Tectonic release: regional propagation effects

We initiated an investigation of the effect on high frequency regional phase propagation of explosion sources associated with components of tectonic stress release. These experiments were inspired in part by the work of Bukchin et al., 2001. That study jointly inverted P wave first motions and teleseismic Love and Rayleigh wave spectra for unconstrained moment tensors of earthquakes and nuclear tests in the Lop Nor region. The amount of tectonic release of nuclear tests was expressed as an angle given by the inverse tangent of the ratio of the isotropic to non-isotropic moment tensor components. The experimental series incorporated moment tensors reported by Bukchin et al. for the Lop Nor 1996-06-08 nuclear tests, although the source location used was that of the southern Xinjian 2003-03-13 earthquake. Envelopes were synthesized for paths to stations MAK and WUS. Additional event mechanisms and locations, including experiments in which depths of tectonic release vary, are available on our group's wiki web link (rainbow.phys.uconn.edu/geowiki).

For this series of experiments, we used the moment tensor decompositions of several explosion events published by Bukchin et al. as our starting points. Although they treat the isotropic and deviatoric components as vertically separated, in these runs we treated them as collocated and coherent (meaning a single moment tensor specifies the entire source, as opposed to running the deviatoric and isotropic source radiation events separately and summing the synthetics). We found that separations of the explosion and tectonic release components as large of 4 km did not visibly affect coda envelopes.

Figure 24 shows an example of one of our event simulations compared to data recorded in several narrow bandpassed filters for 1 to 4 Hz. Note that the P/Lg ratio for the explosion with tectonic release is largest in the lowest frequency band of 1 Hz. This ratio, however, is also typical of that found for explosions without tectonic release at 1 Hz, even though this example is one of the nuclear tests for which Bukchin et al. determined the largest amount of tectonic release, primarily constrained from teleseismic surface waves. In higher frequency bands, excitation of P coda is much larger than Lg, suggesting that event discrimination based on P/Lg ratios will not suffer in bands 2 Hz and higher. This behavior will be strongly affected by the intrinsic Q for shear waves in the crust. We have assumed a $Q_p = 2000$ and $Q_s = 1000$ in the crust. Even though the assumed shear Q is quite high it is still low enough that any Lg trapped in the crust from the explosion is strongly attenuated at this distance range at frequencies 2 Hz and higher.

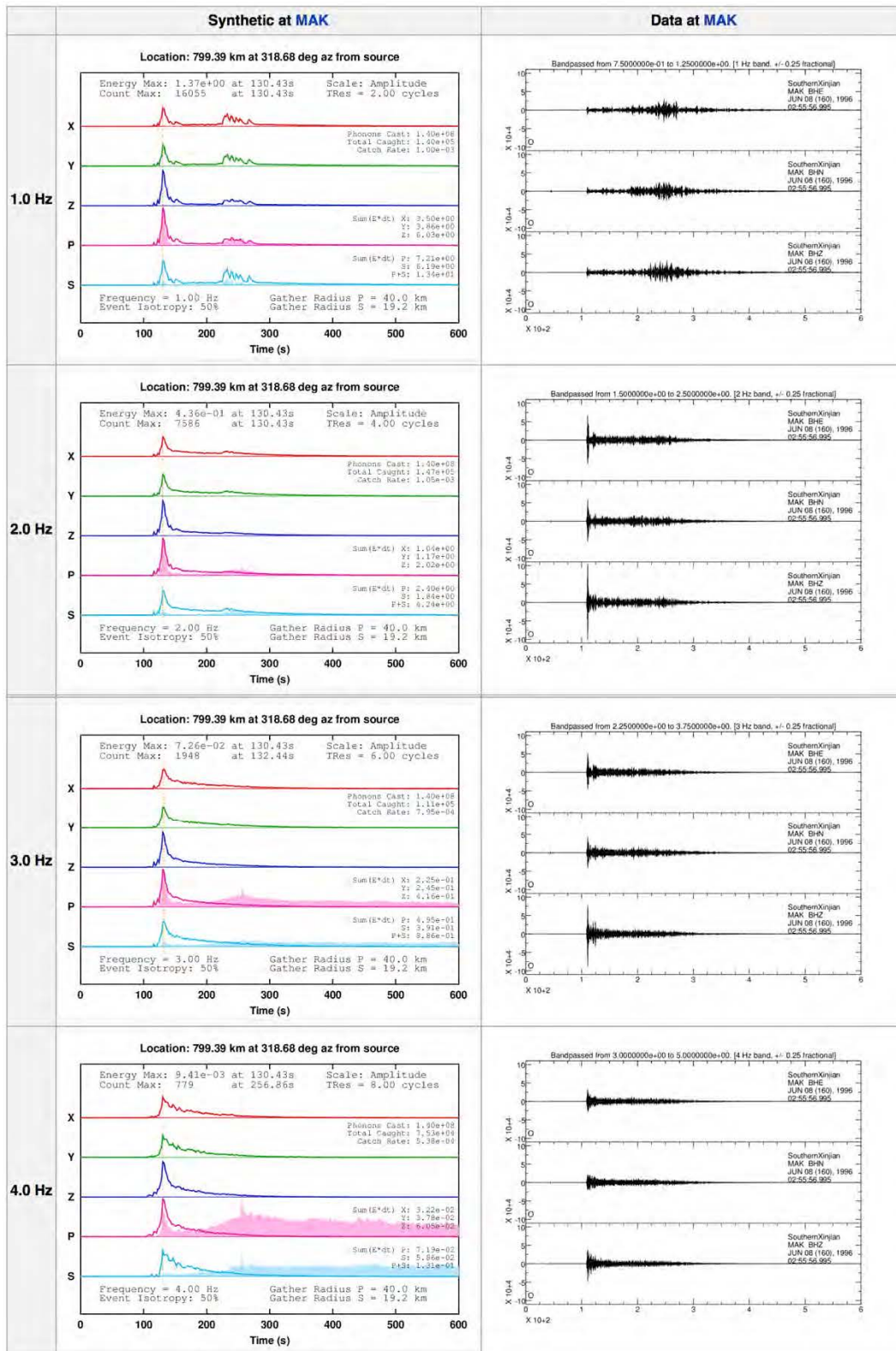


Figure 24. Synthetic coda envelopes for nuclear tests with tectonic release compared with observed data for Lop Nor nuclear tests at a series of narrow frequency bands. *Synthetic envelopes (left) and observed data (right) for Lop Nor nuclear tests as a function of frequency.*

5. CONCLUSIONS

We have developed a radiative transport code to shoot body wave rays through general deterministic 3-D structure, including the computation of quantities required to synthesize high frequency body wave coda generated by small-scale, statistically described heterogeneity. Representing the wavefield as a sum of multiply scattered P and S waves in 3-D, it includes reflection/transmission/P-S conversion by interfaces, effects on the amplitude and polarization of scattered re-radiated waves by from statistically described small-scale heterogeneity, and intrinsic viscoelastic attenuation. Velocity gradients and earth curvature are handled by the ability to include thin layers and an earth-flattening transformation. Development of an option to handle complex 3-D gradients and generalized boundary topography in the large-scale background model is nearly complete, with velocity gradients and topography defined from model values at tetrahedral knots.

Coda envelopes can be plotted in several styles: (1) as a function of time and component of motion at a single station, (2) as a function of distance and time to assist in travel-time picking and travel-time uncertainty estimates, or (3) as snapshots in time as a function of depth and range to understand the evolution of P and S energy and the homogenization of radiation pattern.

Source radiation patterns can be input in the form of generalized moment tensors, which can include tectonic release. The effect of source spectra shape on coda envelopes can be handled by varying the scalar moment for each frequency in simulations for individual narrow bandpassed simulation.

The availability of both explosion and earthquake waveforms, detailed maps of regional phase efficiency, and the existence of 3-D deterministic structural models derived from global stations and transportable arrays make the Lop Nor region an ideal region to implement our modeling technique. In this region we have completed modeling experiments that have tested the effects on regional coda of parameters specifying the heterogeneity spectrum, the effects of crustal and mantle intrinsic attenuation, the effect of a thin sediment layer, the nature of the Moho transition, and the effects and detection of explosion triggered tectonic release. Tests varying the parameters specifying small-scale heterogeneity find that the strongest effects on regional codas occur when the scale length specifying the corner of a von Karman spectrum are close to the dominant wavelength of a narrow bandpassed simulation. P_n and S_n amplitudes strongly depend on velocity gradients and structural complexity beneath the Moho. Accurate estimates of intrinsic Q in the crust are critical input to the modeling of L_g and the prediction of P/L_g ratios. Tectonic release detected from low frequency, teleseismic, surface waves minimally affects the high frequency (>2 Hz) regional coda in the Lop Nor region. Thus far, the most significant conclusion of all of these tests is that performance of discriminants based on P/L_g amplitude ratios is best at frequencies above 2 Hz from recordings at ranges less than 1000 km.

REFERENCES

- Aki, K. and Chouet, B., Origin of coda waves: Source, attenuation, and scattering effects, *J. Geophys. Res.*, **80**, 1975, pp. 3322-3342.
- Aki, K. and Richards, P.G., Quantitative Seismology, Theory and Methods, Vols. I and II. Freeman, New York, N.Y., 1980.
- Allmann, B. P., Shearer, P.M., and Hauksson, E., Spectral discrimination between quarry blasts and earthquakes in southern California, *Bull. Seismol. Soc. Am.*, **98**, 2008, 2073-2079, doi: 10.1785/0120070215.
- Anderson, D.L., Theory of the Earth, 1989, Blackwell, Boston, MA.
- Baumgardt, D.R., Sedimentary basins and blockage of Lg wave propagation in continents, *Pure and Appl. Geophys.*, **158**, 2001, pp.1207-1250.
- Brune, J.N., Tectonic Stress and the Spectra of Seismic Shear Waves from Earthquakes, *J. Geophys. Res.*, **75**, 1970, p. 499.
- Bukchin, B.G., Mostinsky, A.Z., Egorkin, A.A., Levshin, A.L., and Ritzwoller, M.H., Isotropic and nonisotropic components of earthquakes and nuclear explosions at the Lop Nor test site, China, *Pure Appl. Geophys.*, **158**, 2001, pp. 1497-1515.
- Chandrasekhar, S., Radiative Transfer, Dover, 1960, New York, N.Y.
- Cao, S. and K.J. Muirhead, Finite difference modeling of Lg blockage, *Geophys. J. Int.*, **115**, 1993, pp. 85-96.
- Cerveny, V. and Ravindra, R., Theory of Seismic Head Waves, 1971, Univ. of Toronto Press.
- Cormier, V.F. and Anderson, T.S., Efficiency of Lg propagation from SmS ray tracing in three-dimensionally varying crustal waveguides, *Pure and Appl. Geophys.*, **161(8)**, 2004, pp. 1613-1633.
- Cormier, V.F., Attanayake, J., and He, K., Inner core freezing and melting: constraints from seismic body waves, *Phys. Earth Planet Int.*, **188**, 2011, pp. 163-172, doi: 10.1016/j.pepi.2011.07.007.
- Fan, G-W., Lay, T., and Bottone, S., Path corrections for source discriminants: a case study at two international monitoring stations, *Pure Appl. Geophys.*, **159**, 2002, pp. 651-678.
- Fisk, M., Source Spectral Modeling of Regional P/S Discriminants at Nuclear Test Sites in China and the Former Soviet Union, *Bull. Seism. Soc. Am.*, 2006, **96**, pp. 2348-2367, doi:10.1785/0120060023.
- Frankel, A. and Clayton, R.W., Finite difference simulations of seismic scattering: implications for the propagation of short-period seismic waves in the crust and models of crustal heterogeneity, *J. Geophys. Res.*, **91**, 1986, pp. 6465-6489.
- Goff, J.A., Holliger, K., and Levander, A., Modal fields: A new method for characterization of random seismic velocity heterogeneity, *Geophys. Res. Letters*, **21**, 1994, pp. 493-496.
- Gudmundson, O. and Sambridge, M., A regionalized upper mantle (RUM) seismic model, *J. Geophys. Res.*, **103**, 1998, pp. 7121-7136.
- Hedlin, M.A.H., Shearer, P.M., and Earle, P.S., Seismic evidence for small-scale heterogeneity throughout Earth's mantle, *Nature*, **387**, 1997, pp. 145-150.

- Hong, T.-K. and Wu, R.-S., Scattering of elastic waves in geometrically anisotropic media and its implication to sounding of heterogeneity in Earth's deep interior, *Geophys. J. Int.*, **163**, 2005, pp. 324-338.
- Hong, T.-K., Kennett, B.L.N., and Wu, R.-S., Effects of the density perturbation in scattering, *Geophys. Res. Lettr.*, 2004, **31**, 10.1029/2004GL019933.
- Kennett, B.L.N., Engdahl, E.R., and Buland, R., Constraints on seismic velocities in the Earth from travel times, *Geophys. J. Int.*, **122**, 1995, pp.108-124.
- Laske, G., Masters, G., and Reif, C., Crust 2.0: A New Global Crustal Model at 2x2 Degrees, 2011, <http://igppweb.ucsd.edu/~gabi/crust2.html>.
- Levander, A., England, R.W., Smith, S.K., Hobbs, R.W., Goff, J.A., and Holliger, K., Stochastic characterization and seismic response of upper and middle crustal rocks based on the Lewisian Gneiss Complex, Scotland, *Geophys. J. Int.*, **119**, 1994, pp. 243-259.
- Margerin, L., Introduction to radiative transfer of seismic waves, In: *Seismic Data Analysis and Imaging With Global and Local Arrays*, AGU Monograph Series, 2004.
- Mayeda, K., m_b (LgCoda): A stable single station estimator of magnitude, *Bull. Seism. Soc. Am.*, **83**, 1993, pp. 851-861.
- Menke, W., Case Studies of Seismic Tomography in a Regional Context, 2002, <http://www.iris.edu/software/downloads/plotting/>.
- Mueller, R.A. and Murphy, J.R., Seismic characteristics of underground nuclear detonations: Part I. Seismic spectrum scaling, *Bull. Seism. Soc. Am.*, **61**, 1971, pp. 1675-1692.
- Nielsen, L. and Thybo, H., Identification of crustal and upper mantle heterogeneity by modeling of controlled-source seismic data, *Tectonophysics*, **416**, 2006, pp. 208-228.
- Pedersen, H.A., Avouac, J-P., and Campillo, M., Anomalous surface waves from Lop Nor nuclear explosions: observations and numerical modeling, *J. Geophys. Res.*, **103**, 1998, pp. 15,051-15,068.
- Phillips, W.S., Hartse, H.E., Taylor, S.R., Velasco, A.A., and Randall, G.E., Regional phase amplitude tomography for seismic verification, LA-UR-99-635, 1999.
- Przybilla, J., Wegler, U., and Korn, M., Estimation of crustal scattering parameters with elastic radiative transfer theory, *Geophys. J. Int.*, **178**, 2009, doi:10.1111/j.1365-246X.2009.04204.x.
- Pullammanappallil, S., Levander, A., and Larkin, S.P., Estimation of stochastic crustal parameters from seismic exploration data, *J. Geophys. Res.*, **102**, 1997, pp. 15,269-15,286.
- Ruzaikin, A.I., Nersesov, I.L., and Khalturin, V.I., Propagation of Lg and lateral variations in crustal structure in Asia, *J. Geophys. Res.*, **82(2)**, 1971, pp. 307-316.
- Sato H. and Fehler, M.C., Seismic Wave Propagation and Scattering in the Heterogeneous Earth, 1998, Springer-Verlag, New York, N.Y.
- Sens-Schonfelder, C., Margerin, L., and Campillo, M., Laterally heterogeneous scattering explains Lg blockage in the Pyrenees, *J. Geophys. Res.*, **114**, 2009, B07309, doi:10.1029/2008JB006107.
- Shearer, P.M. and Earle, P.S., The global short-period wavefield modeled with a Monte Carlo seismic phonon method, *Geophys. J. Int.*, **158**, 2004, pp. 1103-1117.

- Shearer, P. M. and Earle, P.S., In: *Advances in Geophysics*, Volume 50: Earth Heterogeneity and Scattering Effects on Seismic Waves, H. Sato and M.C. Fehler (ed.), 2008.
- Sykes, L. R. and Nettles, M., Dealing with hard-to-identify seismic events globally and those near nuclear test sites, *International Scientific Studies Conference, Comprehensive Nuclear-Test-Ban Treaty Organization Preparatory Commission*, paper no. SEISMO-26/J, 2009.
- Taylor, S.R., Velasco, A.A., Hartse, H.E., Phillips, W.S., Walter, W.R., and Rodgers, A.J., Amplitude corrections for regional seismic discriminants, *Pure Appl. Geophys.*, **159**, 2002, pp. 623-650.
- Tkalcic, H., Cormier, V.F., Kennett, B.L.N., and He, K., Steep reflections from the Earth's core reveal small-scale heterogeneity in the upper mantle, *Phys. Earth Planet. Int.*, 178, 2010, pp. 80-91, doi: 10.1016/j.pepi.2009.08.004.
- Walter, W. R., Mayeda, K., and Patton, H. J., Phase and spectral ratio discrimination between NTS earthquakes and explosions Part 1: Empirical observations, *Bull. Seism. Soc. Am.*, **85**, 1995, pp. 1050-1067.
- Walter, W.R., Matzel, E., Pasyanos, M.E., Harris, D.B., Gok, R., and Ford, S.R., Empirical observations of earthquake-explosion discrimination using P/S ratios and implications for the sources of explosion S-waves, 29th Monitoring Research Review: Ground-based Nuclear Explosion Technologies, report of contract no. W-7405-ENG-48, 2009.
- Wu, R.S., Multiple scattering and energy transfer of seismic waves — separation of scattering effect from intrinsic attenuation — I. Theoretical modelling. Theoretical modeling, *Geophys. J. R. Astr. Soc.*, **82**, 1985, pp. 57-80.

List of Symbols, Abbreviations, and Acronyms

AFRL	Air Force Research Laboratory
CLVD	Compensated Linear Vector Dipole
DP	Dipole Projection
IMS	International Monitoring Station
IRIS	Incorporated Research Institutions for Seismology
IRIS-DMC	IRIS Data Management Center
LANL	Los Alamos National Laboratory
LLNL	Lawrence Livermore National Laboratory
MFP	Mean Free Path
PNE	Peaceful Nuclear Explosion
PSDF	Power Spectral Density Function

DISTRIBUTION LIST

DTIC/OCP 8725 John J. Kingman Rd, Suite 0944 Ft Belvoir, VA 22060-6218	1 cy
AFRL/RVIL Kirtland AFB, NM 87117-5776	2 cys
Official Record Copy AFRL/RVBYE/Dr. Robert Raistrick	1 cy

This page is intentionally left blank.